EZH2 Inhibition Induces a Metabolic Stress Response Sensitizing TNBC to Glutaminase Targeting

Lucas Porras[1,2], Marina Carrière[3,4], Ann-Sophie Gironne[1,5], Elise Quadri[1,2], Gabriel Alzial[1,2], Hugo Philippeau[1,2], Yousef Aleassa[1,5], Annie Monast[3], Faustine Gorse[1,6], Myriame Saint-Arnaud[1,5], Mariana De Sa Tavares Russo[3], Sylvie Mader[1,2,6], Daina Avizonis[3], Sébastien Lemieux[1,6], Morag Park[3,4], and Geneviève Deblois[1,2,3,5,7*].

[1] Institute for Research in Immunology and Cancer (IRIC), Université de Montréal, Montréal, QC H3C 3J7, Canada.

[2] Department of Molecular Biology, Faculty of Medicine, Université de Montréal, Montréal, QC H3C 3J7, Canada.

[3] Rosalind & Morris Goodman Cancer Institute, McGill University, Montréal, QC H3A 1A3, Canada.

[4] Department of Biochemistry, Faculty of Medicine, McGill University, Montréal, QC H3A 1A3, Canada.

[5] Faculty of Pharmacy, Université de Montréal, Montréal, QC H3C 3J7, Canada.

[6] Department of Biochemistry, Faculty of Medicine, Université de Montréal, Montréal, QC H3C 3J7, Canada.

[7] Lead contact.

* To whom correspondence should be addressed.

Email: genevieve.deblois@umontreal.ca

Keywords: EZH2, dsRNA, integrated stress response, ATF4, amino acid dependency, Glutaminase, Glutaminase inhibitor, triple-negative breast cancer.

The authors declare no potential conflicts of interest.

ABSTRACT

EZH2, the catalytic subunit of Polycomb Repressive Complex II, is overexpressed and associated with poor prognosis in triple-negative breast cancer (TNBC). Although EZH2 inhibition induces significant changes in chromatin landscapes and gene expression, it has a limited impact on the growth of TNBC models, suggesting adaptive compensatory mechanisms. Here, we demonstrate that EZH2 inhibition leads to the accumulation of misfolded proteins and double-stranded RNA (dsRNA), triggering an essential integrated stress response (ISR) through PKR and PERK activation. By inducing ISR-mediated ATF4 activation, EZH2 inhibition enhances amino acid flux and promotes glutaminolysis, in turn activating mTOR signaling to support TNBC cell survival. Pharmacological targeting of this metabolic adaptation with a glutaminase (GLS) inhibitor in combination with EZH2 inhibition significantly impairs TNBC cell proliferation and tumor growth. These findings reveal a stress-driven metabolic adaptation that sustains TNBC survival upon EZH2 blockade and highlight inhibition of this pathway as a strategy to enhance the efficacy of EZH2 inhibitors in TNBC.

INTRODUCTION

Epigenetic reprogramming underlies key tumorigenic processes, including epithelial-to-mesenchymal transition (EMT)[1], immune evasion[2], metastasis[3], and drug resistance[4–6]. Epigenetic regulators thus represent promising therapeutic targets to disrupt tumor progression. The Polycomb Repressive Complexes 1 and 2 (PRC1/PRC2) are key components of the Polycomb Group (PcG) proteins, which regulate chromatin accessibility by forming facultative heterochromatin domains[7]. PRC2 establishes transcriptionally repressive chromatin states through the methylation of histone H3 at lysine 27 (H3K27me1/2/3), a reaction catalyzed by its SET domain-containing methyltransferases Enhancer of Zeste Homolog 1 and 2 (EZH1/EZH2). PcG complexes are crucial for cell-fate determination during embryogenesis and differentiation[8].

Dysregulation of PcG-mediated silencing, due to mutations or aberrant expression, is common in cancer[9,10] and has been associated with tumorigenesis[11]. EZH2 is frequently overexpressed in solid tumors, including breast, ovarian, endometrial, prostate, liver, lung cancers, and melanoma, and is assocaited with metastasis and drug resistance[12,13]. Somatic mutations in EZH2 are predominantly observed in hematologic malignancies, with gain-of-function mutations driving oncogenic activity in lymphomas[14] and loss-of-function mutations linked to tumor suppressor activity in T-cell leukemias and myelodysplastic syndromes[15,16]. Additionally, EZH2 activity is regulated by post-translational modifications, microRNAs, and cofactor interactions, some of which occur independently of PRC2, underscoring the complexity of EZH2 signaling in tumors. Although EZH2 represents an attractive anticancer target, in vivo preclinical studies have shown variable inhibitor activity and frequent resistance. More pronounced effects are observed in hematologic malignancies, particularly germinal-center lymphomas with EZH2 mutations, adult T-cell leukemia/lymphoma, and multiple myeloma[17–19]. By contrast, preclinical solid-tumor models show limited benefit from EZH2 inhibition, with clearer responses in specific genetic backgrounds[20,21]. The EZH2 inhibitor tazemetostat (TAZVERIK) was approved for epithelioid sarcoma and for relapsed/refractory follicular lymphoma with EZH2 mutation[22], and has demonstrated modest activity with durable responses in a subset of patients[23]. The variable response to EZH2 inhibition observed in preclinical studies may reflect adaptive tumor biology, including the rewiring of DNA-damage responses, metabolism, and immune signaling[24–30], supporting rational combination strategies with EZH2 inhibitors as the path forward.

76 In breast cancer, EZH2 is overexpressed in the basal-like subtype, enriched for Triple-Negative
77 Breast Cancer (TNBC), a highly aggressive subtype negative for estrogen and progesterone
78 receptors, and HER2 amplification, which shows high relapse rates following chemotherapy[31].
79 Elevated *EZH2* expression in basal-like breast tumors is associated with advanced stages,
80 chemoresistance, metastasis, and poor prognosis[32–34]. Yet, as observed in other solid malignancies,
81 targeting EZH2 in preclinical TNBC models often yields modest effects on tumor growth despite
82 complete loss of H3K27me[5,6,32]. This limited efficacy suggests the activation of compensatory
83 mechanisms sustaining tumor growth, leading to tolerance to EZH2 inhibition. Understanding the
84 molecular consequences of EZH2 inhibition in TNBC is needed to derive rational combination-
85 based EZH2-targeting strategies[35].

86 Here, we investigate the molecular consequences of targeting EZH2 in TNBC to uncover
87 vulnerabilities that could be exploited to impair tumor growth. We show that pharmacological
88 inhibition or depletion of EZH2 induces an integrated stress response (ISR) in TNBC cells and
89 patient-derived xenografts (PDXs). Specifically, we demonstrate that epigenetic reprogramming
90 induced by EZH2 inhibition activates an essential Integrated Stress Response (ISR) driven by the
91 accumulation of misfolded proteins and double-stranded RNA (dsRNA), which activate Protein
92 Kinase R (PKR) and Protein Kinase RNA-Like Endoplasmic Reticulum Kinase (PERK), and
93 subsequent induction of Activating Transcription Factor-4 (ATF4). By triggering ATF4-dependent
94 transcriptional signatures, EZH2 inhibition enhances amino acid flux and promotes
95 glutaminolysis, in turn activating mTOR signaling and promoting glutathione-mediated
96 antioxidant defense to support TNBC cell survival and tumor growth. Importantly,
97 pharmacological inhibition of this metabolic adaptation with a glutaminase (GLS) inhibitor
98 significantly enhances the efficacy of EZH2 inhibition, providing a strategy to improve TNBC
99 response to EZH2 targeting.

100

101 **RESULTS**

102 **EZH2 Inhibition Activates the Integrated Stress Response via PERK and PKR in TNBC.**

103 Given that EZH2 is overexpressed and associated with aggressive phenotypes in TNBC, we
104 investigated the molecular consequences of its inhibition to identify adaptive responses and
105 potential vulnerabilities. Consistent with prior observations[5], treatment of TNBC PDXs
106 (GCRC1915 and GCRC1939) with the EZH1/2 inhibitor UNC1999 (300 mg/kg, 21 days) does not
107 significantly affect tumor growth (Fig. **1A**), despite robust reduction of H3K27me3 levels by
108 immunoblotting and IHC (Fig. **1B-C**, **S1A-C**), and shows no induction of Cleaved Caspase-3 (Fig.
109 **S1D-E**). In line with prior studies[36], global H3K27ac levels, associated with accessible chromatin,
110 are increased following EZH2 inhibition and H3K27me3 loss in TNBC PDX models. Comparable
111 results were observed in TNBC cell lines MDA-MB-436 and Hs 578T following treatment with
112 UNC1999 or the EZH2-selective inhibitor EPZ-6438 (1 μM, 96 h) (Fig. **1D-E** and **S1F-H**), as well
113 as upon CRISPR/Cas9-mediated EZH2 deletion in MDA-MB-436 cells (Fig. **S1I-K**).

114 To investigate the epigenetic reprogramming induced by EZH2 inhibition in TNBC, we performed
115 chromatin immunoprecipitation sequencing (ChIP-seq with exogenous *Drosophila* DNA spike-in
116 normalization) for H3K27me3 and H3K27ac in TNBC PDX and cells. A significant decrease in
117 the intensity and number of H3K27me3 loci is observed in GCRC1915 PDX exposed to UNC1999
118 in vivo (300 mg/kg, 21 days) compared to vehicle controls (Fig. **1F**; $p < 0.0001$), accompanied by
119 a significant global increase in H3K27ac signal intensity and peak number ($p < 0.0001$)
120 (Fig. **1G**, **S1L**). Genomic regions that lose H3K27me3 upon UNC1999 in TNBC PDXs are
121 globally associated with increased H3K27ac (Fig. **1H**; $r = -0.3905$; $p < 0.0001$), indicating
122 coordinated epigenetic remodeling upon EZH2 inhibition. H3K27ac peaks gained following EZH2
123 inhibition are preferentially enriched at distal intergenic and intronic regions (51.4% distal vs. 33%
124 proximal-promoter), compared with untreated PDX, where H3K27ac is more promoter-proximal
125 (44.6% distal vs. 50% proximal-promoter) (Fig. **1I**), while H3K27me3 peaks show the expected
126 Polycomb-associated distribution across distal intergenic and intronic regions (62.1%) (Fig. **S1M**).
127 Similar results were obtained in MDA-MB346 cells (Fig. **SN-P**). Collectively, these results reveal
128 increased chromatin accessibility at distal non-coding regions following EZH2 inhibition in
129 TNBC.

130 The persistence of TNBC growth despite extensive epigenetic rewiring prompted us to assessed
131 the functional consequences of this epigenetic shift. We analyzed transcriptional changes
132 following EZH2 inhibition in TNBC PDX models and cell lines. Gene set enrichment analysis
133 (GSEA) of genes upregulated following UNC1999 treatment in TNBC PDXs shows significant
134 enrichment of stress-associated pathways (Gene Ontology (GO) Biological Pathways), including
135 ischemia, amino acid transport, ROS and superoxide metabolism, interferon signaling, cholesterol
136 and fatty acid biosynthesis, and endoplasmic reticulum (ER) stress (Fig. **1J**). We next assessed
137 whether some of these stresses are induced upon EZH2 inhibition in TNBC. Using the
138 tetraphenylethene maleimide (TPE-MI) thiol probe, which detects free cysteine thiols, we observe
139 the accumulation of misfolded proteins, a hallmark of endoplasmic reticulum (ER) stress,
140 following exposure to UNC1999 or EPZ-6438 in TNBC cells (Fig. **1K-L** and **S2A-B**). We also
141 observe that EZH2 inhibition induces the production of double-stranded RNA (dsRNA), a
142 hallmark of interferon signaling, a stress-responsive innate immune pathway. Indeed, RNA-seq
143 reveals increased expression of non-coding transposable elements (TEs) in UNC1999-treated
144 TNBC PDXs, particularly Long Terminal Repeat (LTR; ERV1, ERVL/K) and LINE-1 (L1)
145 families (Fig. **1M**, **S2C**). These TEs, which can form dsRNA upon derepression, are enriched in
146 intergenic/intronic non-coding regions that gain accessibility following EZH2 inhibition in TNBC
147 PDX (Fig. **S2D**). Accordingly, dsRNA accumulation detected by immunofluorescence using the
148 J2 antibody is significantly increased following EZH2 inhibition in TNBC PDXs (Fig. **1N-O** and
149 **S2E;** UNC1999, 300 mg/kg) and MDA-MB436 cells (Fig. **1P-Q;** UNC1999/EPZ-6438, 1 μM, 48
150 h). Together, these observations indicate that EZH2 inhibition in TNBC triggers epigenetic
151 rewiring that induces cellular stresses, including misfolded protein and dsRNA accumulation.

152 Accumulation of dsRNA is known to activate Protein Kinase R (PKR) signaling, while misfolded
153 proteins are canonical triggers of the PKR-like endoplasmic reticulum kinase (PERK) arm of the
154 unfolded protein response (UPR) (Fig. **1R**). PERK and PKR phosphorylate the eukaryotic
155 initiation factor 2α (eIF2α) to activate the integrated stress response (ISR), a conserved signaling
156 pathway that reprograms translation and gene expression. This includes preferential translation of
157 Activating Transcription Factor 4 (ATF4), which promotes restoration of cellular homeostasis or
158 adaptive survival under stress. Consistent with this, EZH2 inhibition induces activation of PKR
159 (pT446-PKR), PERK (pT980-PERK), and eIF2α (pS51-eIF2α), along with robust induction of
160 ATF4, in TNBC PDX models (GCRC1915, GCRC1939; Fig. **1S-T** and **S2F-H**; UNC1999, 300

161 mg/kg) and in TNBC cell lines, including MDA-MB-436 (Fig. **1U-V**; UNC1999 or EPZ-6438, 1
162 μM, 48 h) and Hs 578T (Fig. **S2I-J**), as assessed by immunoblotting or IHC. Induction of ATF4
163 is also observed in EZH2-KO MDA-MB-436 cells compared to sgCtl cells (Fig. **S2K-L**).
164 Together, these data establish that EZH2 inhibition drives extensive epigenetic reprogramming in
165 TNBC, triggering PERK- and PKR-dependent activation of the integrated stress response.

166 **The Activation Integrated Stress Response Supports TNBC Cell Survival upon EZH2**
167 **Inhibition.**

168 Since EZH2 inhibition activates stress responses without impairing TNBC growth, we next
169 assessed the functional role of ISR induction by depleting core ISR components with independent
170 siRNAs in MDA-MB-436 and Hs578T cells (Fig. **2A**, **S2M**). Depletion of PERK, PKR, or eIF2α
171 had minimal effects on basal cell viability in TNBC cells but significantly reduced cell viability
172 specifically upon UNC1999 treatment (1 μM, 96 h) (Fig. **2B** and **S2N**). Similarly, siRNA-mediated
173 depletion of ATF4 modestly reduced viability under basal conditions (10–25%) but resulted in a
174 profound loss of viability (80–95%) and robust induction of the apoptotic marker cleaved PARP
175 (cl-PARP) upon EZH2 inhibition in MDA-MB-436, Hs578T (Fig. **2C-E**; UNC1999, 1 μM, 96 h).
176 Similar results were observed with GCRC1915 patient-derived cells exposed to UNC1999 (1 μM;
177 Fig. **2F-G**). Consistent with these genetic perturbations, pharmacologic restoration of eIF2B
178 activity using the Integrated Stress Response Inhibitor (ISRIB; 100 nM), which counteracts the
179 inhibitory effects of pS51-eIF2α, significantly sensitized TNBC cells to EZH2 inhibition (Fig.
180 **2H**), inducing the apoptotic marker cl-PARP (Fig. **2I-J**; UNC1999, 1 μM, 96 h). Collectively,
181 these findings demonstrate that ISR signaling induction supports TNBC cell survival under EZH2
182 inhibition.

183 **EZH2 inhibition induces an ATF4-dependent Amino Acid Metabolic Transcriptional**
184 **Program in TNBC.**

185 Given that ISR activation supports TNBC survival upon EZH2 inhibition, we next investigated the
186 downstream mechanisms by which this stress program promotes cell viability. GSEA of
187 differentially expressed genes in GCRC1915 PDX and MDA-MB-436 cells exposed to UNC1999
188 had revealed significant enrichment of previously defined ATF4 target genes, including amino
189 acid transporters and metabolic enzymes implicated in redox homeostasis (Fig. **1J** and **S3A**).
190 Consistent with this enrichment, EZH2 inhibition using UNC1999 in GCRC1915 PDX models

191 (300 mg/kg) significantly increased the expression of genes enriched in amino acid transport,
192 antioxidant defense, and amino acid metabolism (Fig. **3A** and **S3B**). Immunoblotting and
193 immunohistochemical analyses confirmed the significant induction of key amino acid transporters
194 (LAT1/SLC7A5, CD98/SLC3A2, ASCT2/SLC1A5, xCT/SLC7A11) and metabolic enzymes
195 (PSAT1, BCAT1, ASNS) at the protein level following EZH2 inhibition in both GCRC1915 PDX
196 and TNBC cell lines (Fig. **3B-E** and **S3C-E**). To determine whether this response depends on
197 induction of ATF4 in response to EZH2 inhibition, we depleted ATF4 using independent siRNAs
198 in MDA-MB-436 cells. We observed that loss of ATF4 significantly attenuated the UNC1999-
199 dependent induction of these transporters and metabolic enzymes in TNBC cells (Fig. **3F-G** and
200 **S3F-G**).

201 Transcriptomic profiling further demonstrated that genes downregulated upon ATF4 depletion in
202 EZH2-inhibited cells are significantly enriched for ISR-related pathways, including PERK and
203 amino acid metabolism (Reactome, FDR $q < 0.05$; Fig. **3H-I**). Notably, genes induced by
204 UNC1999 treatment in TNBC cells show a significant inverse correlation with gene expression
205 changes following ATF4 depletion (Fig. **3J**), including multiple amino acid transporters and
206 metabolic enzymes involved in redox homeostasis (Fig. **3K**). In contrast, ATF4 depletion leads to
207 upregulation of gene signatures associated with senescence, apoptosis, oxidative stress, and
208 ferroptosis (Fig. **S3H**), consistent with a protective role for ATF4 under EZH2 inhibitory stress.
209 Finally, chromatin immunoprecipitation followed by qPCR demonstrates that EZH2 inhibition
210 promotes ATF4 recruitment to the promoters of representative amino acid transport and
211 metabolism genes, including *ASNS*, *BCAT1*, *PSAT1*, and *SLC7A11*, in GCRC1915 PDX and
212 MDA-MB-436 cells (Fig. **3L**), supporting a direct transcriptional regulatory role. Together, these
213 results demonstrate that EZH2 inhibition engages ATF4 to induce a transcriptional program
214 centered on amino acid metabolism and redox homeostasis in TNBC.

215 **EZH2 Inhibition Activates an Amino Acid-Dependent Metabolic Rewiring in TNBC.**

216 Given the ATF4-dependent induction of amino acid transport and metabolic genes following
217 EZH2 inhibition, we next assessed whether this program translates into functional changes in
218 amino acid handling in TNBC cells. Quantification of metabolites in conditioned media from
219 MDA-MB-436 and Hs 578T cells revealed a significant increase in glutamine uptake and
220 glutamate release following treatment with UNC1999 or EPZ-6438 (1μM; 72 h), while glucose

221 uptake and lactate secretion remained unchanged (Fig. **4A** and Fig. **S4A**; Nova BioProfile 400
222 analyzer). Targeted amino acid profiling using LC-QQQ-MS further demonstrated that EZH2
223 inhibition enhances uptake of branched-chain amino acids (leucine, valine, isoleucine), serine,
224 methionine, glutamine, and cystine, accompanied by increased glutamate release (Fig. **4B** and Fig.
225 **S4B**). These metabolic changes are consistent with the engagement of amino acid transporters,
226 including LAT1 and the xCT/CD98 antiporter system, which are upregulated following EZH2
227 inhibition (Fig. 3A-B). The xCT/CD98 complex couples cystine import to glutamate export,
228 thereby supporting glutathione synthesis and antioxidant defense. In line with this model, uptake
229 of glutamine and branched-chain amino acids can replenish intracellular glutamate through
230 transamination reactions, while serine and methionine contribute to glutathione biosynthesis and
231 redox-related metabolic pathways (Fig. **4C**). Importantly, depletion of ATF4 significantly
232 attenuated EZH2 inhibitor-induced amino acid uptake in MDA-MB-436 cells, indicating that these
233 metabolic changes are ATF4-dependent (Fig. **4D**).

234 Because the mammalian/mechanistic target of rapamycin (mTOR) complex 1 (mTORC1)
235 signaling is highly sensitive to intracellular amino acid availability, we next evaluated its activation
236 following EZH2 inhibition in TNBC cells and observed increased phosphorylation of the
237 downstream Ribosomal Protein S6 Kinase (S6K) target S6 (pS235/236-S6; Fig. **4E-F**). Consistent
238 with mTORC1 activation, EZH2 inhibition increased phosphorylation of the direct S6K1 substrate
239 carbamoyl-phosphate synthetase 2, aspartate transcarbamylase, and dihydroorotase enzyme
240 (CAD, pS1859-CAD), which couples mTORC1-driven amino acid sensing to de novo pyrimidine
241 synthesis. Furthermore, EZH2 inhibition by UNC1999 (1μM) further impaired MDA-MB436 and
242 Hs 578T cell growth in combination with pharmacological inhibition of mTOR signaling using
243 rapamycin (mTORC1-selective) or Torin1 (dual mTORC1/2 inhibitor), indicating that mTOR
244 signaling contributes to growth-supportive response upon EZH2 inhibition in TNBC cells (Fig.
245 **4G**).

246 LC-QTOF-MS analysis further reveals increased intracellular levels of glutamate, α-ketoglutarate
247 (αKG), oxidized glutathione, asparagine, fumarate, and malate in TNBC cells treated with
248 UNC1999 (1 μM, 72 h) (Fig. **4H** and Fig. **S4C**), consistent with changes in amino acid uptake and
249 utilization and engagement of redox-associated metabolic pathways. Stable isotope tracing with
250 $^{13}C_5$-glutamine demonstrates significantly increased incorporation of glutamine-derived carbon
251 into glutamate and α-ketoglutarate upon EZH2 inhibition in TNBC cells, indicative of enhanced

252 glutaminolysis, while carbon flux into the oxidative branch of the TCA cycle is modestly reduced
253 with a corresponding increase in reductive carboxylation-derived metabolites (Fig. **4I** and Fig.
254 **S4D-E**). No change in glutamine-derived labeling of GABA is observed, indicating that this
255 alternative anaplerotic route is not engaged (Fig. **S4F**). Despite these metabolic changes, Seahorse
256 analysis revealed no significant alterations in basal or stress-induced oxygen consumption or
257 extracellular acidification rates (OCR, ECAR), suggesting that EZH2 inhibition does not induce
258 broad bioenergetic rewiring in TNBC cells (Fig. **S4G-H**).

259 Given the increased cystine uptake, enhanced glutaminolysis, glutamate availability and release,
260 and accumulation of oxidized glutathione following EZH2 inhibition, we next tested whether
261 TNBC cells become functionally dependent on glutathione-dependent redox homeostasis under
262 these conditions. Inhibition of the glutathione-synthesizing enzyme glutamate–cysteine ligase with
263 buthionine sulfoximine (BSO) significantly reduced TNBC cell viability, specifically when treated
264 with UNC1999 (1 μM), revealing a metabolic vulnerability associated with induced amino acid-
265 and redox-related adaptations upon EZH2 inhibition (Fig. **4J**). Together, these results demonstrate
266 that EZH2 inhibition engages an ATF4-dependent amino acid metabolic program that activates
267 mTOR signaling and redox-maintenance, thereby supporting TNBC cell growth and fitness under
268 EZH2-inhibitory stress.

269 **Glutaminase Targeting Sensitizes TNBC to EZH2 Inhibition.**

270 To determine whether the observed enhancement of glutamine metabolism is functionally required
271 under EZH2 inhibition, we assessed TNBC cell viability under glutamine-replete or glutamine-
272 limited conditions. EZH2 inhibition with UNC1999 (1 μM) selectively reduces cell viability under
273 low-glutamine conditions (0.08 mM), while cells remain relatively insensitive in glutamine-replete
274 media (4 mM), indicating increased glutamine dependency upon EZH2 inhibition (Fig. **5A**).
275 Consistent with this phenotype, EZH2 inhibition using UNC1999 or EPZ-6438 (1μM)
276 significantly increases the expression of glutaminase (GLS), the enzyme catalyzing the first step
277 of glutaminolysis, in TNBC cell lines (Fig. **5B-C**). GLS levels are also elevated in EZH2-deleted
278 TNBC cells (Fig. **S5A-B**) and in TNBC PDX models (GCRC1915 and GCRC1939) treated with
279 UNC1999, as assessed by immunoblotting and immunohistochemistry (Fig. **5D-E** and Fig. **S5C**).
280 Importantly, independent siRNA-mediated depletion of ATF4 significantly blunts UNC1999-

281 induced GLS upregulation in TNBC cells, indicating that ATF4 induction contributes to GLS
282 increase downstream of EZH2 inhibition (Fig. **5F-G**).

283 To directly assess the functional contribution of GLS in the response to EZH2 inhibition, we
284 depleted GLS using independent siRNAs (Fig. **5H** and **S5D**) and observed a pronounced
285 sensitization of TNBC cells to EZH2 inhibition (UNC1999/EPZ-6438, 1 μM, 120 h). Likewise,
286 pharmacological inhibition of GLS using the clinically relevant inhibitor telaglenastat (CB-839)
287 similarly sensitized multiple TNBC cell lines and patient-derived cells to EZH2 inhibition (Fig. **5I**
288 and Fig. **S5E** UNC1999/EPZ-6438, 1 μM, 120 h), as well as EZH2-deficient cells (Fig. **S5F**),
289 indicating that loss of EZH2 function creates a dependency on glutaminase activity.
290 Mechanistically, GLS inhibition attenuated EZH2 inhibitor-induced activation of mTOR
291 signaling, as evidenced by reduced phosphorylation of pS235/236-S6 and pS1859-CAD,
292 supporting a model in which enhanced glutaminolysis sustains mTOR-dependent growth signaling
293 following EZH2 inhibition (Fig. **5J-K**).

294 Finally, to evaluate its therapeutic relevance in vivo, we treated mice bearing GCRC1915 TNBC
295 PDX tumors with UNC1999 (150 mpk), CB-839 (200 mpk), or the combination. Combined EZH2
296 and GLS inhibition significantly reduced tumor growth compared to single-agent treatments,
297 without affecting body weight (Fig. **5L-M** and Fig. **S5G**). Tumor analyses revealed robust
298 induction of apoptotic markers, including cleaved PARP and cleaved caspase-3, specifically in the
299 combination-treated group (Fig. **5N-P**), with no corresponnding increase in apoptosis or stress
300 markers observed in normal tissues (Fig. **S5H**). Similar sensitization to GLS inhibition was
301 observed in xenografts derived from EZH2-deleted TNBC cells (Fig. **S5I-L**). Together, these
302 findings demonstrate that EZH2 inhibition induces an ATF4-dependent glutamine metabolic
303 rewiring that creates a selective dependency on glutaminase activity and that targeting this
304 vulnerability markedly sensitizes TNBC cells and tumors to EZH2 inhibition.

305 **DISCUSSION**

306 This study defines a coordinated adaptive response of TNBC cells to EZH2 inhibition, linking
307 epigenetic perturbation to cellular stress signaling and metabolic reprogramming. Although EZH2
308 inhibition induces widespread epigenetic changes and elicits multiple stress responses that are
309 potentially deleterious to cancer cells, including misfolded proteins and dsRNA accumulation, it
310 does not uniformly impair TNBC cell viability, proliferation, or tumor growth. Instead, we show
311 that TNBC cells adapt to EZH2-inhibitory stress by engaging an ISR that supports cellular fitness
312 and proliferative capacity. Central to this response is ISR-driven ATF4 induction, which promotes
313 a metabolic rewiring characterized by enhanced amino acid uptake and glutaminolysis, thereby
314 supporting glutathione-dependent redox homeostasis and mTOR activation to sustain TNBC cell
315 growth upon EZH2 inhibition. Importantly, we demonstrate that disrupting this adaptive metabolic
316 response, specifically by targeting glutaminolysis through GLS inhibition, selectively sensitizes
317 TNBC cells and tumors to EZH2 inhibition, revealing a therapeutically exploitable vulnerability.

318 EZH2 is emerging as a promising therapeutic target in cancer due to its central role in regulating
319 gene expression and cell identity through histone modifications. It has been implicated in cell
320 proliferation, invasion, migration, drug resistance and senescence, underscoring its significance in
321 tumor progression[25,37,38]. The development of pharmacological EZH2 inhibitors has therefore
322 garnered considerable attention, as exemplified by the FDA approval of tazemetostat
323 (TAZVERIK®) for epithelioid sarcoma and follicular lymphoma[22]. Recent studies have
324 highlighted the context-dependent nature of EZH2 targeting, as its inhibition does not uniformly
325 suppress tumor growth and, in certain settings, may even promote tumorigenesis[39]. The tumor
326 microenvironment further modulates EZH2 activity, with hypoxia and inflammation regulating
327 EZH2 expression through HIF-1α[40] and NF-κB/STAT3[41] signaling pathways, while nutrient
328 availability can influence its activity via metabolic changes[42]. Adding another layer of complexity,
329 EZH2 also exhibits PRC2-independent functions that have been described in TNBC and may
330 persist despite pharmacological inhibition, thereby contributing to tumorigenesis through
331 alternative mechanisms[43]. Whether such non-canonical EZH2 activities contribute to the ISR-
332 ATF4-driven metabolic reprogramming identified in this study remains an important question for
333 future investigation. Collectively, these observations underscore the need for a comprehensive
334 understanding of the multifaceted and context-dependent roles of EZH2 across cancer types to
335 optimize therapeutic strategies and minimize unintended consequences.

336 EZH2 inhibition induces broad epigenetic remodeling in TNBC, characterized by loss of
337 H3K27me3 and compensatory gains in H3K27ac at promoters and intergenic regions, consistent
338 with prior reports linking this epigenetic switch to adaptive transcriptional programs that activate
339 oncogenic pathways[35,44]. In our models, this remodeling is accompanied by misfolded protein
340 accumulation, ER stress signatures, as well as increased expression of transposable elements,
341 dsRNA and induction of innate immune-associated stress signatures, including interferon-related
342 pathways. In some tumor contexts, induction of this signature can potentiate the antitumor activity
343 of EZH2 inhibition[45] and enhance sensitivity to immunomodulatory therapies when amplified[46–
344 48]. However, these responses are not sufficient to impair tumor growth in TNBC. Instead, our data
345 indicate that these epigenetic stress outputs act as upstream stress signals that converge on ISR
346 activation, which ultimately determines cellular fitness following EZH2 inhibition. This
347 framework helps reconcile why EZH2 inhibitors can elicit ER stress and dsRNA or immune-
348 related transcriptional programs without uniformly inducing cell-intrinsic cytotoxicity and
349 suggests that epigenetic stress alone is insufficient to drive tumor regression in the absence of
350 targeted disruption of adaptive stress-response pathways. Targeting compensatory epigenetic
351 adaptations has emerged as an effective strategy to enhance responses to EZH2 inhibition[49].
352 Consistent with this concept, co-inhibition of chromatin regulators such as bromodomains, p300,
353 MLL, HDACs, PRMT1, or DNMTs has been shown to synergize with EZH2 inhibitors across
354 multiple cancer models by suppressing adaptive transcriptional programs and promoting pro-
355 apoptotic gene expression[35,50,51]. These findings underscore the therapeutic potential of rational
356 epigenetic combination strategies to overcome the intrinsic adaptability of cancer cells to PRC2
357 inhibition and highlight the need to identify context-specific dependencies that dictate response to
358 EZH2-targeted therapies.

359 ATF4 is a central transcriptional effector of the integrated stress response, coordinating cellular
360 adaptation to nutrient limitation, proteotoxic stress, and redox imbalance[52]. In cancer, ATF4 has
361 been shown to support survival and therapy resistance by regulating amino acid metabolism, redox
362 homeostasis, and stress-adaptive transcriptional programs[53]. Our data identify ATF4 as a key
363 integrator of EZH2 inhibitor-induced stress in TNBC, linking epigenetic perturbation to metabolic
364 reprogramming and altered amino acid utilization. While additional stress-responsive transcription
365 factors may contribute to this response, our findings place ATF4-mediated metabolic adaptations
366 at the center of the adaptive program that sustains cellular fitness under EZH2-inhibitory

367 conditions. Notably, ATF4 has also been implicated in apoptotic signaling under conditions of
368 severe or prolonged stress[54], suggesting that the balance between adaptation and cell death
369 following EZH2 inhibition is likely context-dependent and shaped by the magnitude and duration
370 of ISR activation.

371 Metabolic rewiring is increasingly recognized as a consequence of EZH2 inhibition across cancer
372 models[27,28]. Here, we demonstrate that in TNBC, EZH2 inhibition induces a stress-driven
373 dependence on glutamine metabolism that can be therapeutically exploited. Given the limited
374 specificity and clinical tractability of direct ISR or ATF4 inhibitors, we prioritized targeting
375 glutaminase (GLS) as a downstream, druggable node of this adaptive metabolic program.
376 Telaglenastat (CB-839), a clinically advanced GLS1 inhibitor, has shown activity in TNBC but
377 with heterogeneous responses (#NCT02071862; NCT03057600)[55], underscoring the need for
378 predictive tumor contexts that define GLS dependency. Our findings indicate that EZH2 inhibition
379 creates such a context, rendering TNBC cells and tumors selectively vulnerable to GLS inhibition.
380 Whether additional EZH2-GLS combinations (eg, IACS-6274, BPTES) could refine efficacy
381 remains to be investigated. Co-targeting EZH2 and glutamine metabolism, therefore, represents a
382 rational strategy to enhance therapeutic efficacy, potentially reduce EZH2 inhibitor dosing, and
383 broaden the clinical benefit of GLS-targeted therapies in TNBC.

384 Together, this study reframes EZH2 inhibition in TNBC as a stress-adaptive process rather than
385 intrinsically cytotoxic therapy, revealing how cellular fitness is preserved through metabolic
386 rewiring. By uncovering a targetable glutamine dependency that arises from this adaptation, our
387 findings provide a conceptual and therapeutic framework for rational combination strategies that
388 overcome stress tolerance and enhance the efficacy of epigenetic therapies in triple-negative breast
389 cancer.
390

391 **KEY RESOURCES AND AVAILABILITY**

392 Detailed information on reagents is provided in the Supplemental Materials and Methods. Further
393 information and requests for reagents should be directed to the lead contact, Geneviève Deblois
394 (genevieve.deblois@umontreal.ca).

395 **EXPERIMENTAL MODEL AND STUDY PARTICIPANT DETAILS**

396 **Cell culture**. TNBC PDX-derived cells (GCRC1915 PDC) and the Hs 578T and MDA-MB-436
397 lines were maintained at 37°C in 5% CO_2. Hs 578T and MDA-MB-436 were cultured in
398 Dulbecco's Minimal Eagle's Medium (DMEM) with 10% dialyzed FBS and 1%
399 penicillin/streptomycin. GCRC1915 PDCs were cultured in Ham's F12/DMEM (25:75) with 5%
400 dialyzed FBS, 0.4 µg/mL hydrocortisone, 5 µg/mL insulin, 10 ng/mL EGF, 8.4 ng/mL cholera
401 toxin, 50 µM ROCK inhibitor, and 50 µg/mL gentamycin. Cells were treated in vitro with
402 UNC1999 (1 µM), EPZ-6438 (1 µM), Rapamycin (1 nM), Torin1 (1 nM), various doses of ISRIB,
403 BSO, or CB-839, all dissolved in DMSO.

404 **Animal studies**. All patient tissue samples were collected with informed consent under REB-
405 approved protocols at McGill University Health Centre and Jewish General Hospital (SUR-2000-
406 966; CER 2022-4027). Mice were maintained according to institutional animal care guidelines
407 (SUR-99-780; 2014-7514). TNBC PDX tumors (GCRC1915 and GCRC1939) were cryopreserved
408 in F12-DMEM with FBS and 10% DMSO at –80°C. Tumor fragments (~1 mm^3) were transplanted
409 subcutaneously into the mammary fat pad of 5–7-week-old female non-obese diabetic scid gamma
410 (NSG) mice. For cellular xenografts, 7.5×10^5 Hs 578T cells were transplanted in 1:1 Matrigel.
411 When tumors reached ~150 mm^3, mice were randomized to receive vehicle, UNC1999 (150–300
412 mg/kg, 5×/week), CB-839 (200 mg/kg, daily), or the combination. Tumor volume was measured
413 using calipers [(length × $width^2$)/2], and mice were sacrificed when tumors reached 2000–2500
414 mm^3. UNC1999 and CB-839 were formulated in Sodium carboxymethyl cellulose (NaCMC) and
415 (2-Hydroxypropyl)-β-cyclodextrin (HP-β-CD) with Tween 80, respectively.

416 **METHOD DETAILS**

417 **RNA Extraction and Sequencing**. PDX samples were collected after 21 days of treatment with
418 or without UNC1999. Hs 578T and MDA-MB-436 cells were treated with EZH2 inhibitors (4

419 days) or siATF4 (2 days). RNA was extracted using Qiagen RNeasy kits, quantified with Qubit,
420 and quality-checked on an Agilent Bioanalyzer. Poly-A-enriched or ribo-depleted RNA libraries
421 were prepared with the KAPA RNA HyperPrep kit and sequenced on Illumina NextSeq500 (SE,
422 74–84 bp) or Novaseq (PE, 100 bp). Reads were trimmed with Trimmomatic and aligned to a
423 hybrid human (GRCh38/Gencode37) and mouse (GRCm38/GencodeM25) genome using STAR.
424 Human gene counts were normalized and analyzed for differential expression with DESeq2 (FDR
425 < 0.05), and normalized counts were further used for functional enrichment analyses using GSEA
426 with hallmark and GO biological pathways.

427 **Protein Extraction and Immunoblotting Analysis**. Whole-cell pellets were lysed in buffer
428 containing 50 mM Tris-HCl (pH 7.5), 150 mM NaCl, 1% Triton X-100, 0.1% SDS, and 0.5%
429 sodium deoxycholate, sonicated (QSonica Q700, 4°C, 80% amplitude, 10 cycles of 30 s ON/30 s
430 OFF), and quantified by Lowry assay. Proteins (20–40 µg) were separated on 8–12% SDS-PAGE
431 gels and transferred to PVDF membranes (Trans-Blot Turbo, BioRad). Membranes were blocked
432 with 5% milk or 3% BSA in TBS-T for 1 hour, incubated with primary antibodies overnight at
433 4°C, and detected using HRP-conjugated secondary antibodies and Clarity ECL substrate
434 (BioRad).

435 **siRNA Transfection**. Cells were seeded and transfected 4 hours later with siRNA (20 nM) using
436 the siLentFect lipid reagent (BioRad) according to the manufacture's protocol for a total duration
437 of 48-72 h. 2 siRNAs/gene were used against *EIF2A2*/PKR, *EIF2A3*/PERK, *EIF2A/*eIF2α, *ATF4*,
438 and non-Targeting siRNA ("si-Control" 1 and 2) were used as a negative control.

439 **Lentivirus preparation and generation of stable cell lines**. MDA-MB-436 and Hs 578T EZH2
440 knockout cells were generated using lentiviral transduction. Cells were first transduced with
441 lentiCas9-Blast and selected with blasticidin (10 µg/mL, 7 days). Two different sgRNAs targeting
442 EZH2 exons 4 and 5, or a non-targeting control sgRNA (lenti-sgRNA puro), were then introduced
443 and cells were selected with puromycin (1 µg/mL, 7 days). Lentiviral particles were produced in
444 HEK 293T cells by co-transfecting psPAX2 and pVSV.G with the Cas9 or sgRNA vectors. EZH2
445 depletion was validated by immunoblotting.

446 **Chromatin Immunoprecipitation**. Chromatin was prepared from UNC1999-treated PDX
447 GCRC1915 tumors (300 mg/kg, 6×/week) and MDA-MB-436 cells (1 μM, 4 days) or vehicle
448 controls. Cells and tissues were crosslinked with 1% formaldehyde (10 min), and chromatin was
449 sonicated (QSonica Q700, 4°C, 80% amplitude, 35 cycles of 30 s ON/30 s OFF) to
450 approximatively 400 bp fragments. Immunoprecipitation was performed with 50 μg chromatin and
451 4 μg antibody for H3K27me3/H3K27ac and 300 μg chromatin and 1 μg antibody for ATF4.
452 Drosophila spike-in antibody (2 μg) was used with 50 μg of chromatin for histone mark
453 normalization. IgG and input controls were included. ATF4 ChIP enrichment was verified by
454 qPCR at *ASNS*, *SLC7A11*, *BCAT1*, and *PSAT1* loci (primer sequences listed in Supplemental
455 Materials and Methods) using SensiFast SYBR. Purified DNA was quantified by Qubit and used
456 to generate sequencing libraries (KAPA DNA HyperPrep Kit). Libraries were sequenced paired-
457 end 100 bp, except one PDX replicate sequenced single-end 84 bp. ChIP-seq reads were aligned
458 to human (GRCh38 Gencode40), mouse (GRCm39 GencodeM29), and Drosophila (BGDP.28)
459 reference genomes to distinguish species-specific reads. Only uniquely mapped or properly paired
460 reads were retained, and duplicates or low-quality reads (MAPQ < 30) were removed. Peaks were
461 called using MACS3 with default FDR thresholds, using the --broad flag for H3K27me3. Spike-
462 in normalization using Drosophila reads was applied to BigWig visualizations, and differential
463 binding for H3K27ac samples was analyzed using DiffBind with DESeq2. Peak annotation and
464 visualization were performed using ChIPseeker and deepTools.

465 **Transposable element expression.** TE analysis included Salmon index generation, TE expression
466 quantification and subfamily enrichment. TE sequences were extracted from RepeatMasker
467 annotations, combined with transcriptomes, and indexed in Salmon for locus-specific
468 quantification in human and mouse. TE annotations were refined using RepeatMasker, HMMER,
469 and the Dfam database. Differential expression analysis was performed at the locus level using
470 DESeq2, filtering for human TE insertions with sufficient read coverage. Subfamily enrichment
471 was assessed by comparing differentially expressed TE insertions to the full annotated set using
472 Fisher's exact test. For full experimental and computational details, including all parameters,
473 commands, and scripts, see the Supplemental Materials and Methods.

474 **Fixed cells immunofluorescence**. Cells were plated on glass-bottom dishes, treated as indicated,
475 fixed with methanol, permeabilized with Triton X-100, and blocked with PBS-T containing 3%

476 BSA. Cells were incubated overnight at 4°C with anti-dsRNA antibody (1:100), followed by
477 Alexa647-conjugated secondary antibody (1:500) and DAPI (300nM) nuclear staining. Images
478 were acquired using a Leica SP8 confocal microscope and analyzed with ImageJ. dsRNA
479 fluorescence intensity was quantified in 15 cells per biological replicate and normalized to DMSO-
480 treated controls; IgG was used as a negative control.

481 **Tissue processing, immunohistochemistry and immunofluorescence and imaging**. Four-
482 micrometer sections were prepared from formalin-fixed, paraffin-embedded PDX tissues.
483 Immunohistochemistry was performed using automated deparaffinization and antigen retrieval on
484 a Discovery XT stainer, followed by primary antibody incubation using the Bond Polymer DAB
485 Refine Kit on a Bond RX stainer and hematoxylin counterstaining. Slides were scanned using a
486 NanoZoomer system and images were extracted with NDP Scan software. For
487 immunofluorescence, sections were manually deparaffinized, rehydrated, and subjected to antigen
488 retrieval in citrate buffer (pH 6.0). After blocking, sections were incubated overnight at 4°C with
489 anti-dsRNA (1:50) and anti-H3K27me3 (1:100) antibodies, followed by Alexa488- and Alexa647-
490 conjugated secondary antibodies (1:500) and DAPI (30nM) nuclear staining. Slides were imaged
491 using a Cytation 5 system (20× objective). Image analysis was performed using QuPath, with cell
492 identification based on DAPI intensity and nuclear morphology. Mean dsRNA signal intensity
493 ratios were calculated and averaged across three biological replicates per condition.

494 **Proliferation assays**. Cells were seeded in 96-well black plates (≥3 technical replicates) and
495 incubated with AlamarBlue reagent (1:25, 3 h) on days 0, 3, and 6. Fluorescence was measured at
496 590 nm using a Spark® multimode plate reader, and relative growth was calculated as a ratio to
497 day 0 for each condition.

498 **Viability assays**. Cells were plated in 96-well plates (3 technical replicates) and treated as
499 indicated. After treatment, cells were fixed with 100% cold methanol (10 min) and stained with
500 Crystal Violet. Stained cells were lysed with 0.2% SDS, and absorbance was measured at 592 nm
501 using a Spark® multimode plate reader.

502 **Protein misfolding assays**. Misfolded and unfolded protein levels were measured using the
503 tetraphenyl ethene maleimide (TPE-MI) probe, which fluoresces upon binding free cysteines. Cells

504 were seeded in black 24-well plates and treated with or without EZH2 inhibitors for 48 h, then
505 incubated with TPE-MI (25 μM) for 45 min. After PBS washes, fluorescence was measured at 470
506 nm using a Spark multimode plate reader and cells were imaged using a Cytation 5 system in
507 brightfield and GFP channels.

508 **Extracellular metabolite consumption rate**. Hs 578T and MDA-MB-436 cells were cultured in
509 four independent biological replicates with or without UNC1999 or EPZ-6438. After 3 days,
510 extracellular media were collected to measure glucose (g/L), lactate (g/L), glutamine (mmol/L)
511 and glutamate (mmol/L) levels, and cells were counted for normalization. Media samples were
512 clarified by centrifugation and analyzed using a BioProfile 400 Analyzer (Nova Biomedical).
513 Metabolite concentrations were corrected by subtracting values from naïve media and normalized
514 to cell number to calculate relative uptake or release under treated versus untreated conditions.

515 **Metabolomics and stable isotope tracing.** For amino acid analysis, Hs 578T and MDA-MB-436
516 cells were cultured as described, treated with EZH2 inhibitors for 3 days, and transfected with
517 siControl, siATF4-1, or siATF4-2. Extracellular media were extracted for metabolite analysis
518 using ammonium formate washes and organic solvent extraction. For glutamine tracing, Hs 578T
519 cells were treated with DMSO or UNC1999 for 2 days, then incubated in DMEM containing 4
520 mM $13C_5$-glutamine or unlabeled glutamine for 2 h. Metabolites were extracted from cells as
521 described above. Targeted metabolomics was performed by LC–MS using triple quadrupole
522 MRM, while stable isotope tracer analyses were conducted using high-resolution QTOF mass
523 spectrometry. Metabolites were separated using UHPLC with either ion-pairing reversed-phase
524 chromatography for central carbon metabolites or hydrophilic interaction chromatography for
525 amino acids. Data were normalized to total metabolite signal and analyzed for relative abundance
526 and isotope enrichment. Detailed extraction procedures, chromatographic conditions, instrument
527 parameters, and data analysis methods are provided in the Supplemental Materials and Methods.

528 **Extracellular measurement of oxygen consumption rate.** Cells were treated with EZH2
529 inhibitors for 72 h prior to analysis. Oxygen consumption rate (OCR) and extracellular
530 acidification rate (ECAR) were measured 3–4 times using a Seahorse XF-96 analyzer. Data are
531 presented as OCR (pmol/min/μg protein) and ECAR (mpH/min/μg protein). Basal and maximal
532 respiration were assessed under basal conditions following sequential injection of oligomycin (1

533 μM), FCCP (0.5 μM), and rotenone/antimycin A (0.5 μM) to determine ATP-linked respiration
534 and maximal oxygen consumption.

535 **QUANTIFICATION AND STATISTICAL ANALYSIS**

536 Data are presented as mean ± SD with no exclusions. Statistical analyses were performed using
537 Prism 9 (GraphPad) and included two-tailed Student's t-tests, one-way or two-way ANOVA with
538 post hoc Dunnett's tests, as indicated in figure legends. Analyses assumed normal distribution and
539 equal variances. A P value ≤ 0.05 was considered significant. For in vivo studies, sample sizes
540 were predetermined, and experiments were conducted with blinding.

541 **RESSOURCE AVAILABILITY**

542 Genomic data is available under GSE307150 (elqhmuwyxjgxnsv), GSE307151
543 (wrcfumqslxgllcp), GSE307152 (ilczwwcivzynrqj), GSE307153 (shypoasyhpujzyv), GSE307154
544 (wngpkommttunhmh), GSE307155 (udolsiyappmxnev).

545 Code is available under https://github.com/annsophiegironne/ezh2_paper.

546 Requests for further information and resources should be directed to and will be fulfilled by the
547 lead contact, Geneviève Deblois, Ph.D. (genevieve.deblois@umontreal.ca). Any additional
548 information required to reanalyze the data reported in this paper is available from the lead contact
549 upon request.

550 **AUTHOR CONTRIBUTION**

551 Conceptualization: G.D., M.C., L.P.; Data curation: L.P., A.S.G., G.D.; Formal analyses: A.-S.G.,
552 L.P., M.C., G.D.; Funding acquisition: G.D., M.P.; Investigation: L.P., M.C., E.Q., G.A., H.P.,
553 Y.A., A.M., M.S.-A., M.D.T.R., F.G.,; Methodology: L.P., M.C., G.D., A.-S.G., S.L., D.A.;
554 Resources: G.D., M.P., S.M.; Supervision: G.D.; Writing of original draft: G.D., M.C., L.P.;
555 Review and editing: G.D., L.P., A.-S.G, S.L.
556

ACKNOWLEDGEMENTS

We would like to thank all members of the Deblois lab for technical assistance and scientific input on the manuscript. The authors wish to thank the Institute for Research in Immunology and Cancer (IRIC) Genomic platform (Raphaëlle Lambert and Salwa Haidar) for ChIP-seq and RNA-seq libraries and sequencing, Histology platform (Marianne Isaac and Melina Narlis) for IHC staining. We thank the IRIC Bioinformatics platform for providing the infrastructure and assistance with the analyses. We acknowledge the Fonds de recherche du Québec (FRQ) – secteur Santé for supporting the Institute for Research in Immunology and Cancer (IRIC), an FRQ-designated research center. Metabolomics data were collected by the Metabolomics Innovation Resource (MIR) at the Rosalind and Morris Goodman Cancer Institute, McGill University. MIR is supported by our cost-recovery program, as well as the Terry Fox Research Institute, the Fondation du Cancer du sein du Québec, the Goodman Cancer Institute, and McGill University. (https://www.mcgill.ca/gci/facilities/metabolomics-innovation-resource-mir). This study was conducted with the support of the Canadian Institute for Health Research (CIHR) Funding Reference Number PJT-470501-CPT-CFCA-172840 (to G.D), the Réseau de Recherche en Cancer of the FRQ (to M. Park), Québec Breast Cancer Foundation (to M. Park) and the National Sciences and Engineering Research Council of Canada (to S.M.). G. Deblois is a recipient of a CIHR Early Career Investigator in Cancer award, a Forbeck Scholar and a Research Scholar – Junior2 recipient from the Fonds de Recherche en Santé du Québec. M. Park is a James McGill Professor and holds the Diane and Sal Guerra Chair in Cancer Genetics at McGill University. L.P. M.F. and G.A. are recipients of a Fonds de Recherche en Santé du Québec doctoral scholarship. M.F. is a recipient of a CIHR doctoral studentship and a Canderel Doctoral Scholarship. A-S.G. and Y.A are recipients of a Fonds de Recherche en Santé du Québec Master's scholarship, a CIHR BESC-M Master scholarship, and a Centennial scholarship from the Faculty of Pharmacy of the Université de Montréal.

DECLARATION OF INTERESTS

The authors declare no competing interests.

585 **REFERENCES**

586

587 1. Su, Y. *et al.* Epigenetic reprogramming of epithelial mesenchymal transition in triple negative
588 breast cancer cells with DNA methyltransferase and histone deacetylase inhibitors. *J. Exp.*
589 *Clin. Cancer Res.* **37**, 314 (2018).

590 2. Ratnam, N. M. *et al.* Reversing epigenetic gene silencing to overcome immune evasion in
591 CNS malignancies. *Front. Oncol.* **11**, 719091 (2021).

592 3. Verma, A. *et al.* EZH2-H3K27me3 mediated KRT14 upregulation promotes TNBC
593 peritoneal metastasis. *Nat. Commun.* **13**, 7344 (2022).

594 4. Pineda, B. *et al.* DNA methylation as an epigenetic signature predictive of response to
595 neodjuvant treatment in TNBC patients. *J. Clin. Oncol.* **36**, e12658–e12658 (2018).

596 5. Deblois, G. *et al.* Epigenetic Switch-Induced Viral Mimicry Evasion in Chemotherapy-
597 Resistant Breast Cancer. *Cancer Discov.* **10**, 1312–1329 (2020).

598 6. Marsolier, J. *et al.* H3K27me3 conditions chemotolerance in triple-negative breast cancer.
599 *Nat. Genet.* **54**, 459–468 (2022).

600 7. Comet, I., Riising, E. M., Leblanc, B. & Helin, K. Maintaining cell identity: PRC2-mediated
601 regulation of transcription and cancer. *Nat. Rev. Cancer* **16**, 803–810 (2016).

602 8. Lavarone, E., Barbieri, C. M. & Pasini, D. Dissecting the role of H3K27 acetylation and
603 methylation in PRC2 mediated control of cellular identity. *Nat. Commun.* **10**, 1679 (2019).

604 9. Chase, A. & Cross, N. C. P. Aberrations of EZH2 in cancer. *Clin. Cancer Res.* **17**, 2613–2618
605 (2011).

606 10. Erokhin, M. *et al.* Clinical correlations of Polycomb repressive complex 2 in different tumor
607 types. *Cancers (Basel)* **13**, 3155 (2021).

608 11. Parreno, V. *et al.* Transient loss of Polycomb components induces an epigenetic cancer fate.
609 *Nature* **629**, 688–696 (2024).

610 12. Li, H., Cai, Q., Godwin, A. K. & Zhang, R. Enhancer of zeste homolog 2 promotes the
611 proliferation and invasion of epithelial ovarian cancer cells. *Mol. Cancer Res.* **8**, 1610–1618
612 (2010).

613 13. Bachmann, I. M. *et al.* EZH2 expression is associated with high proliferation rate and
614 aggressive tumor subgroups in cutaneous melanoma and cancers of the endometrium,
615 prostate, and breast. *J. Clin. Oncol.* **24**, 268–273 (2006).

616 14. Morin, R. D. *et al.* Somatic mutations altering EZH2 (Tyr641) in follicular and diffuse large
617 B-cell lymphomas of germinal-center origin. *Nat. Genet.* **42**, 181–185 (2010).

618 15. Gu, Z. *et al.* Loss of EZH2 Reprograms BCAA Metabolism to Drive Leukemic
619 Transformation. *Cancer Discov.* **9**, 1228–1247 (2019).

620 16. Ernst, T. *et al.* Inactivating mutations of the histone methyltransferase gene EZH2 in myeloid
621 disorders. *Nat. Genet.* **42**, 722–726 (2010).

622 17. Zeng, D., Liu, M. & Pan, J. Blocking EZH2 methylation transferase activity by GSK126
623 decreases stem cell-like myeloma cells. *Oncotarget* **8**, 3396–3411 (2017).

624 18. Daisuke, S. *et al.* EZH2 inhibitor DZNep induces apoptosis in adult T-cell
625 leukemia/lymphoma cells by BCL2 suppression via regulation of Mir-181a. *Blood* **122**,
626 4265–4265 (2013).

627 19. Caganova, M. *et al.* Germinal center dysregulation by histone methyltransferase EZH2
628 promotes lymphomagenesis. *J. Clin. Invest.* **123**, 5009–5022 (2013).

629 20. Keller, P. J. *et al.* Comprehensive target engagement by the EZH2 inhibitor tulmimetostat
630 allows for targeting of ARID1A mutant cancers. *Cancer Res.* **84**, 2501–2517 (2024).

631 21. Huang, R., Wu, Y. & Zou, Z. Combining EZH2 inhibitors with other therapies for solid
632 tumors: more choices for better effects. *Epigenomics* **14**, 1449–1464 (2022).

633 22. Hoy, S. M. Tazemetostat: First Approval. *Drugs* **80**, 513–521 (2020).

634 23. Julia, E. & Salles, G. EZH2 inhibition by tazemetostat: mechanisms of action, safety and
635 efficacy in relapsed/refractory follicular lymphoma. *Future Oncol.* **17**, 2127–2140 (2021).

636 24. Piunti, A. *et al.* Immune activation is essential for the antitumor activity of EZH2 inhibition
637 in urothelial carcinoma. *Sci. Adv.* **8**, eabo8043 (2022).

638 25. Chibaya, L. *et al.* EZH2 inhibition remodels the inflammatory senescence-associated
639 secretory phenotype to potentiate pancreatic cancer immune surveillance. *Nat. Cancer* **4**,
640 872–892 (2023).

641 26. Bowen, C. M. *et al.* Inhibition of histone methyltransferase EZH2 for immune interception
642 of colorectal cancer in Lynch syndrome. *JCI Insight* **10**, (2025).

643 27. Nylund, P. *et al.* A distinct metabolic response characterizes sensitivity to EZH2 inhibition
644 in multiple myeloma. *Cell Death Dis.* **12**, 167 (2021).

645 28. Nocito, M. C. *et al.* A targetable antioxidant defense mechanism to EZH2 inhibitors enhances
646 tumor cell vulnerability to ferroptosis. *Cell Death Dis.* **16**, 291 (2025).

647 29. W-M Fan, T. *et al.* Metabolic reprogramming driven by EZH2 inhibition depends on cell-
648 matrix interactions. *J. Biol. Chem.* **300**, 105485 (2024).

649 30. Xu, L. *et al.* Pharmacological inhibition of EZH2 combined with DNA-damaging agents
650 interferes with the DNA damage response in MM cells. *Mol. Med. Rep.* **19**, 4249–4255
651 (2019).

652 31. Bianchini, G., Balko, J. M., Mayer, I. A., Sanders, M. E. & Gianni, L. Triple-negative breast
653 cancer: challenges and opportunities of a heterogeneous disease. *Nat. Rev. Clin. Oncol.* **13**,
654 674–690 (2016).

655 32. Yomtoubian, S. *et al.* Inhibition of EZH2 Catalytic Activity Selectively Targets a Metastatic
656 Subpopulation in Triple-Negative Breast Cancer. *Cell Rep.* **30**, 755-770.e6 (2020).

657 33. De Brot, M., Rocha, R. M., Soares, F. A. & Gobbi, H. Prognostic impact of the cancer stem
658 cell related markers ALDH1 and EZH2 in triple negative and basal-like breast cancers.
659 *Pathology* **44**, 303–312 (2012).

660 34. Yu, Y. *et al.* Epigenetic Co-Deregulation of EZH2/TET1 is a Senescence-Countering,
661 Actionable Vulnerability in Triple-Negative Breast Cancer. *Theranostics* **9**, 761–777 (2019).

662 35. Huang, X. *et al.* Targeting Epigenetic Crosstalk as a Therapeutic Strategy for EZH2-Aberrant
663 Solid Tumors. *Cell* **175**, 186-199.e19 (2018).

664 36. Yamagishi, M. *et al.* Mechanisms of action and resistance in histone methylation-targeted
665 therapy. *Nature* **627**, 221–228 (2024).

666 37. Bai, Y. *et al.* Inhibition of enhancer of zeste homolog 2 (EZH2) overcomes enzalutamide
667 resistance in castration-resistant prostate cancer. *J. Biol. Chem.* **294**, 9911–9923 (2019).

668 38. Luo, C. *et al.* H3K27me3-mediated PGC1α gene silencing promotes melanoma invasion
669 through WNT5A and YAP. *J. Clin. Invest.* **130**, 853–862 (2020).

670 39. Deb, G., Thakur, V. S. & Gupta, S. Multifaceted role of EZH2 in breast and prostate
671 tumorigenesis: epigenetics and beyond. *Epigenetics* **8**, 464–476 (2013).

672 40. Mahara, S. *et al.* HIFI-α activation underlies a functional switch in the paradoxical role of
673 Ezh2/PRC2 in breast cancer. *Proc. Natl. Acad. Sci. U. S. A.* **113**, E3735-44 (2016).

674 41. da Hora, C. C. *et al.* Sustained NF-κB-STAT3 signaling promotes resistance to Smac
675 mimetics in Glioma stem-like cells but creates a vulnerability to EZH2 inhibition. *Cell Death*
676 *Discov.* **5**, 72 (2019).

677 42. Dann, S. G. *et al.* Reciprocal regulation of amino acid import and epigenetic state through
678 Lat1 and EZH2. *EMBO J.* **34**, 1773–1785 (2015).

679 43. Anwar, T., Gonzalez, M. E. & Kleer, C. G. Noncanonical Functions of the Polycomb Group
680 Protein EZH2 in Breast Cancer. *Am. J. Pathol.* (2021) doi:10.1016/j.ajpath.2021.01.013.

681 44. Knutson, S. K. *et al.* A selective inhibitor of EZH2 blocks H3K27 methylation and kills
682 mutant lymphoma cells. *Nat. Chem. Biol.* **8**, 890–896 (2012).

683 45. Hsieh, Y.-Y., Lo, H.-L. & Yang, P.-M. EZH2 inhibitors transcriptionally upregulate cytotoxic
684 autophagy and cytoprotective unfolded protein response in human colorectal cancer cells.
685 *Am. J. Cancer Res.* **6**, 1661–1680 (2016).

686 46. Morel, K. L. *et al.* EZH2 inhibition activates a dsRNA-STING-interferon stress axis that
687 potentiates response to PD-1 checkpoint blockade in prostate cancer. *Nat. Cancer* **2**, 444–456
688 (2021).

689 47. Qiu, F. *et al.* EZH2 inhibition activates dsRNA-interferon axis stress and promotes response
690 to PD-1 checkpoint blockade in NSCLC. *J. Cancer* **13**, 2893–2904 (2022).

691 48. Chomiak, A. A. *et al.* Select EZH2 inhibitors enhance viral mimicry effects of DNMT
692 inhibition through a mechanism involving NFAT:AP-1 signaling. *Sci. Adv.* **10**, eadk4423
693 (2024).

694 49. Kazansky, Y. *et al.* Overcoming clinical resistance to EZH2 inhibition using rational
695 epigenetic combination therapy. *Cancer Discov.* **14**, 965–981 (2024).

696 50. Li, Z. *et al.* Methylation of EZH2 by PRMT1 regulates its stability and promotes breast cancer
697 metastasis. *Cell Death Differ.* **27**, 3226–3242 (2020).

698 51. Zhang, L. *et al.* DNMT and EZH2 inhibitors synergize to activate therapeutic targets in
699 hepatocellular carcinoma. *Cancer Lett.* **548**, 215899 (2022).

700 52. Lines, C. L., McGrath, M. J., Dorwart, T. & Conn, C. S. The integrated stress response in
701 cancer progression: a force for plasticity and resistance. *Front. Oncol.* **13**, 1206561 (2023).

702 53. Wortel, I. M. N., van der Meer, L. T., Kilberg, M. S. & van Leeuwen, F. N. Surviving stress:
703 Modulation of ATF4-mediated stress responses in normal and malignant cells. *Trends*
704 *Endocrinol. Metab.* **28**, 794–806 (2017).

705 54. Matsumoto, H. *et al.* Selection of autophagy or apoptosis in cells exposed to ER-stress
706 depends on ATF4 expression pattern with or without CHOP expression. *Biol. Open* **2**, 1084–
707 1090 (2013).

708 55. Harding, J. J. *et al.* A phase I dose-escalation and expansion study of telaglenastat in patients
709 with advanced or metastatic solid tumors. *Clinical cancer research: an official journal of the*
710 *American Association for Cancer Research* vol. 27 4994–5003 (2021).

711 56. Tameire, F. *et al.* ATF4 couples MYC-dependent translational activity to bioenergetic
712 demands during tumour progression. *Nat. Cell Biol.* **21**, 889–899 (2019).

FIGURE 1

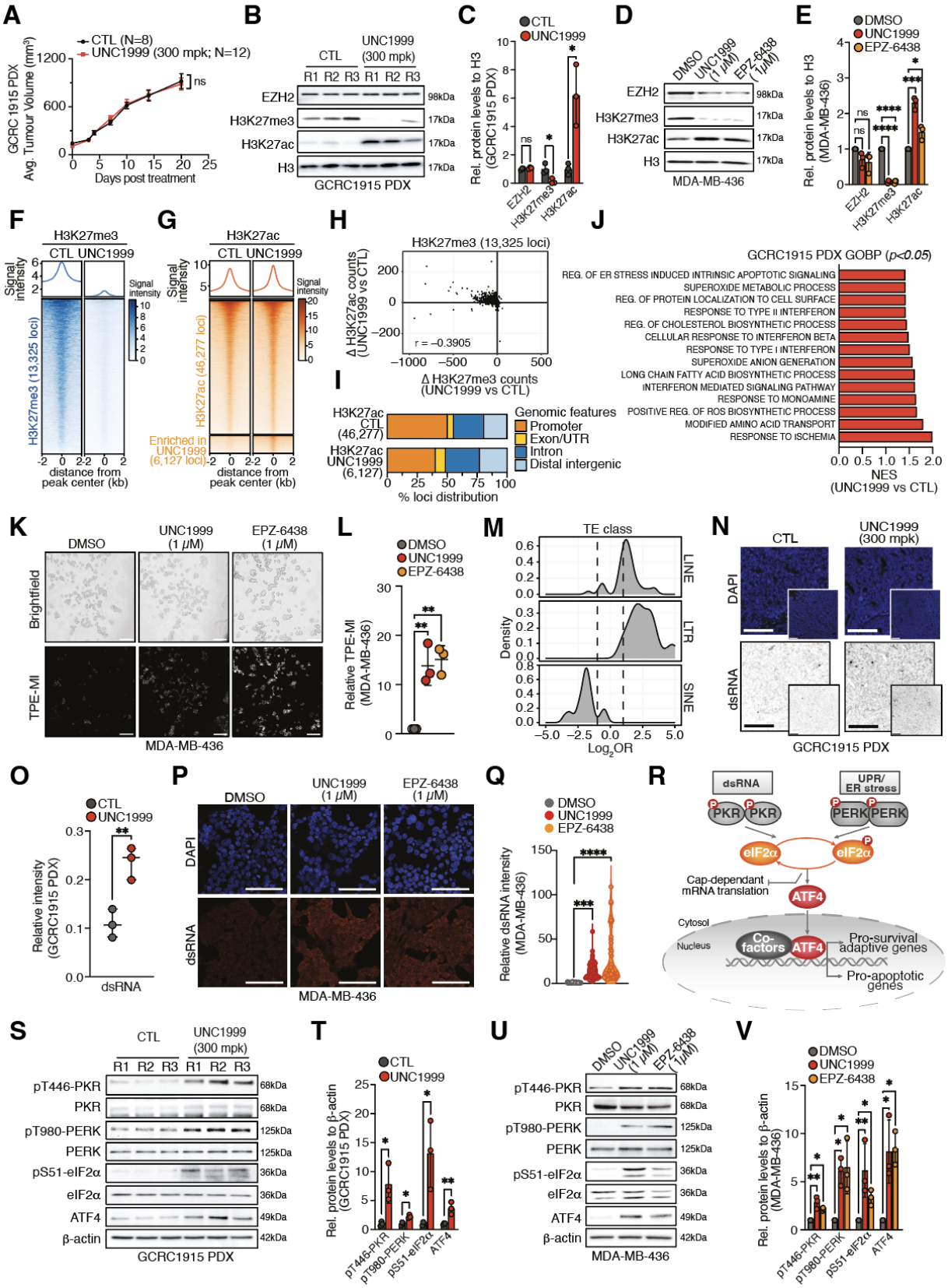
A
CTL (N=8)
UNC1999 (300 mpk; N=12)
GCRC 1915 PDX Avg. Tumour Volume (mm³)
Days post treatment
ns
B
CTL
UNC1999 (300 mpk)
R1 R2 R3 R1 R2 R3
EZH2
H3K27me3
H3K27ac
H3
GCRC1915 PDX
C
CTL
UNC1999
Rel. protein levels to H3 (GCRC1915 PDX)
D
DMSO
UNC1999 (1 μM)
EPZ-6438 (1 μM)
MDA-MB-436
E
DMSO
UNC1999
EPZ-6438
Rel. protein levels to H3 (MDA-MB-436)
F
H3K27me3
CTL UNC1999
Signal intensity
H3K27me3 (13,325 loci)
distance from peak center (kb)
G
H3K27ac
H3K27ac (46,277 loci)
Enriched in UNC1999 (6,127 loci)
H
H3K27me3 (13,325 loci)
Δ H3K27ac counts (UNC1999 vs CTL)
Δ H3K27me3 counts (UNC1999 vs CTL)
r = −0.3905
I
H3K27ac CTL (46,277)
H3K27ac UNC1999 (6,127)
Genomic features
Promoter
Exon/UTR
Intron
Distal intergenic
% loci distribution
J
GCRC1915 PDX GOBP (p<0.05)
REG. OF ER STRESS INDUCED INTRINSIC APOPTOTIC SIGNALING
SUPEROXIDE METABOLIC PROCESS
REG. OF PROTEIN LOCALIZATION TO CELL SURFACE
RESPONSE TO TYPE II INTERFERON
REG. OF CHOLESTEROL BIOSYNTHETIC PROCESS
CELLULAR RESPONSE TO INTERFERON BETA
RESPONSE TO TYPE I INTERFERON
SUPEROXIDE ANION GENERATION
LONG CHAIN FATTY ACID BIOSYNTHETIC PROCESS
INTERFERON MEDIATED SIGNALING PATHWAY
RESPONSE TO MONOAMINE
POSITIVE REG. OF ROS BIOSYNTHETIC PROCESS
MODIFIED AMINO ACID TRANSPORT
RESPONSE TO ISCHEMIA
NES (UNC1999 vs CTL)
K
DMSO
UNC1999 (1 μM)
EPZ-6438 (1 μM)
Brightfield
TPE-MI
MDA-MB-436
L
DMSO
UNC1999
EPZ-6438
Relative TPE-MI (MDA-MB-436)
M
TE class
LINE
LTR
SINE
Density
Log₂OR
N
CTL
UNC1999 (300 mpk)
DAPI
dsRNA
GCRC1915 PDX
O
CTL
UNC1999
Relative intensity (GCRC1915 PDX)
dsRNA
P
DMSO
UNC1999 (1 μM)
EPZ-6438 (1 μM)
DAPI
dsRNA
MDA-MB-436
Q
DMSO
UNC1999
EPZ-6438
Relative dsRNA intensity (MDA-MB-436)
R
dsRNA
UPR/ ER stress
PKR
PERK
eIF2α
Cap-dependant mRNA translation
ATF4
Cytosol
Nucleus
Co-factors
Pro-survival adaptive genes
Pro-apoptotic genes
S
CTL
UNC1999 (300 mpk)
R1 R2 R3 R1 R2 R3
pT446-PKR
PKR
pT980-PERK
PERK
pS51-eIF2α
eIF2α
ATF4
β-actin
GCRC1915 PDX
T
CTL
UNC1999
Rel. protein levels to β-actin (GCRC1915 PDX)
pT446-PKR
pT980-PERK
pS51-eIF2α
ATF4
U
DMSO
UNC1999 (1 μM)
EPZ-6438 (1 μM)
MDA-MB-436
V
DMSO
UNC1999
EPZ-6438
Rel. protein levels to β-actin (MDA-MB-436)

713

714 **Figure 1.** EZH2 Inhibition Induces an Integrated Stress Response Triggered by dsRNA
715 Accumulation and Misfolded proteins in TNBC. **A.** Time-dependent growth curve showing the
716 average tumor volume of GCRC1915 PDX implanted in female NSG mice, exposed to UNC1999
717 (300 mg/kg; 21 days, N=12) or control (N=8). **B.** Immunoblot showing the levels of EZH2,
718 H3K27me3, H3K27ac, and total H3 in GCRC1915 and GCRC1939 PDX exposed or not to
719 UNC1999 (300 mg/kg; 21 days; N=3). **C.** Quantification of the relative protein levels from Fig.1B
720 (rel. to H3; N=3). **D.** Immunoblot showing EZH2, H3K27me3, H3K27ac, and total H3 levels in
721 MDA-MB-436 cells exposed to UNC1999, EPZ-6438 (1 µM, 96 h; N=3) or mock treated (DMSO,
722 0.2%). **E.** Quantification of the relative protein levels from Fig.1D (rel. to H3; N=3). **F.** Heatmap
723 of peak intensity signal of H3K27me3 ChIP-seq peaks (–2 to +2 kb window from peak center)
724 upon control (left) or UNC1999 (300 mg/kg; right) treatment in GCRC1915 PDX (N=3).
725 Compilation of tag density is illustrated for the 13,325 H3K27me3 peaks at the top of each
726 condition. **G.** Heatmap of peak intensity signal of H3K27ac ChIP-seq specific peaks (–2 to +2 kb
727 window from peak center) upon control (left) or UNC1999 (300 mg/kg; right) treatment in
728 GCRC1915 PDX. Boxes illustrate common peaks between control and UNC1999, those specific
729 to control (N=2) or UNC1999 (N=3; >2-fold difference in peak intensity between conditions,
730 $p<0.05$ (DiffBind)). H3K27ac tag density plots are illustrated for the common H3K27ac peaks at
731 the top of heapmaps for each condition. **H.** Scatter plot (Pearson, p-value<0.0001) representing
732 the difference in H3K27ac or H3K27me3 counts on H3K27me3 sites (13,325) following
733 UNC1999 treatment in GCRC1915 PDX (300 mg/kg, 21 days; N=2-3). **I.** Stacked bar charts
734 illustrating the proportion of H3K27ac peaks associated with distinct genomic localization/features
735 relative to gene TSS upon control or UNC1999 treatment in GCRC1915 PDX (300 mg/kg, 21
736 days; N=2-3). **J.** Gene Set Enrichment Analysis (GSEA) graph representing Normalized
737 Enrichment Score (NES) from GOBP (Gene Ontology: Biological Process) gene set, illustrating
738 significantly enriched pathways ($p<0.05$) in UNC1999-treated GCRC1915 PDX relative to control
739 treatment (300 mg/kg; 21 days; N=3). **K.** Detection of misfolded protein load in MDA-MB-436
740 cells exposed to DMSO (0.2%) or EZH2 inhibitors UNC1999 or EPZ-6438 (1µM; 48 h; N=3),
741 using the tetraphenyl ethene maleimide (TPE-MI) probe (IF). Cell density is shown in brightfield.
742 Scale bars, 100µm. **L.** Quantification of misfolded protein load intensity from Fig.1Q showing
743 TPE-MI intensity normalized to naïve media and relative to DMSO (0.2%). **M.** Density chart
744 representing overall enrichment level of significantly upregulated transposable elements (TE)

745 classes in UNC1999-treated GCRC1915 PDX (300 mg/kg; 21 days; N=3) relative to control. Odds
746 ratio (OR) and p-value computed using Fisher's exact test. **N.** Immunofluorescence staining using
747 J2 (dsRNA) antibody in GCRC1915 PDX treated with control or UNC1999 (300 mg/kg; 21 days;
748 N=3). Scale bar, 100µm. **O**. Quantification of dsRNA levels relative to DAPI intensity from
749 Fig.1N (N=3). **P.** Immunofluorescence staining using J2-antibody in MDA-MB436 cells exposed
750 to DMSO (0.2%), UNC1999 or EPZ-6438 (1µM; 48 h; N=3). Scale bar, 100µm. **Q.** J2-staining
751 quantification from Fig.1P using Image J. **R.** Schematic representing the main stresses involved in
752 the activation of the stress kinases PKR and PERK that induce ISR and ISR-mediated activation
753 of eIF2α and ATF4 induction. **S.** Immunoblot showing pT446-PKR, PKR, pT980-PERK, PERK,
754 pS51-eIF2α, eIF2α, ATF4 and β-actin levels in GCRC1915 PDX exposed to control or UNC1999
755 (300 mg/kg; 21 days; N=3). **T.** Quantification of the relative protein levels from Fig.1S (rel. to β-
756 actin; N=3). **U.** Same as in Fig.1S in MDA-MB-436 cells exposed to DMSO (0.2%), UNC1999,
757 or EPZ-6438 (1 µM; 48 h, N=3). **V.** Quantification of the relative protein levels from Fig.1U (rel.
758 to β-actin; N=3). All data shown are mean ± SD for three biological replicates (C, E, L, O, Q, T
759 and V), except for tumor volume (A) where means ± SEM and N=8 (CTL) or 12 (UNC1999) are
760 represented. Statistical analysis was performed using one-way ANOVA (E, L, Q and V) and two-
761 tailed Student's t test (C, O and T). *$p < 0.05$, **$p < 0.01$, ***$p < 0.001$, ****$p < 0.0001$; ns, not
762 significant. R: replicate #.

FIGURE 2

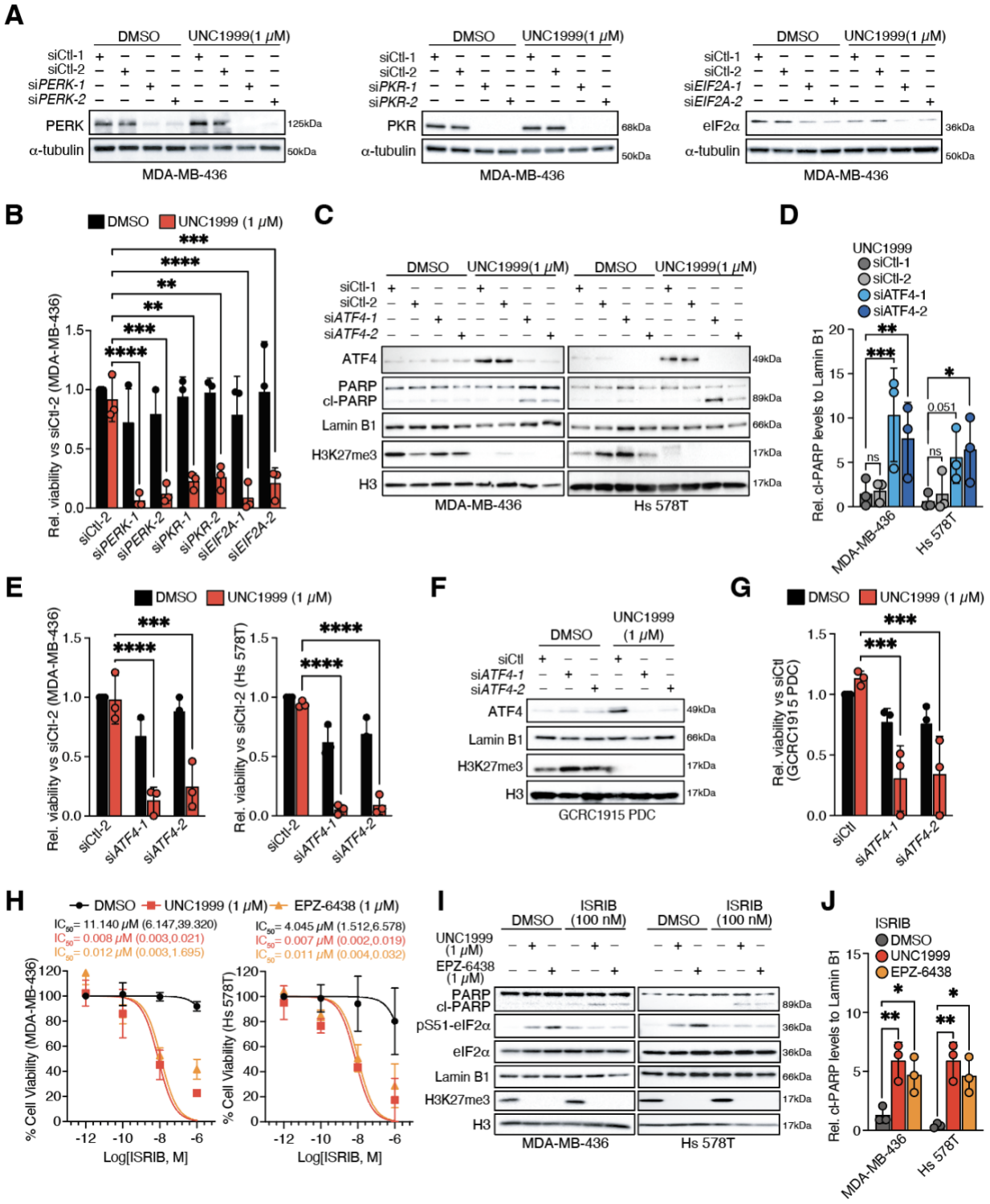

763

764

765 **Figure 2.** Induction of the Integrated Stress Response Supports TNBC Cell Survival upon EZH2
766 Inhibition. **A.** Immunoblot showing the levels of the indicated proteins (PKR, PERK, eIF2α or α-
767 tubulin) in MDA-MB-436 cells exposed to DMSO (0.2%) or UNC1999 (1μM; 48 h, N=3) and
768 depleted or not for the indicated protein using two siRNAs per gene (vs non-targeting siRNAs
769 (siCtl)). **B.** Relative viability (crystal violet) of MDA-MB-436 cells depleted of either PKR, PERK,
770 or eIF2α using siRNAs (vs siControl) and exposed to UNC1999 (1μM; 96 h, N=3) or DMSO
771 (0.2%). **C.** Immunoblot showing the levels of the indicated proteins in MDA-MB-436 and Hs 578T
772 cells exposed to DMSO (0.2%) or UNC1999 (1μM; 72 h; N=3) and depleted of ATF4 using two
773 siRNAs (vs siCtl). **D.** Quantification of the relative protein levels from Fig. 2C (rel. to Lamin B1;
774 N=3). **E.** Relative viability (crystal violet) of MDA-MB-436 and Hs 578T cells depleted of ATF4
775 using siRNAs (vs siCtl) and exposed to UNC1999 (1μM; 96 h) or DMSO (0.2%; N=3). **F.**
776 Immunoblot showing the levels of the ATF4, Lamin B1, H3K27me3 and total H3 proteins in
777 GCRC1915 PDC exposed to UNC1999 (1μM; 48 h) or DMSO (0.2%; N=3) and depleted of ATF4
778 using specific siRNAs (72 h). **G.** Relative viability (crystal violet) of GCRC1915-PDC depleted
779 of ATF4 using 2 siRNAs and exposed to UNC1999 (1μM; 96 h; N=3). **H.** Dose-response curves
780 representing the relative normalized viability of MDA-MB-436 (left) and Hs 578T (right) cells
781 exposed to DMSO (0.2%), UNC1999 or EPZ-6438 (1μM; 96h) (N=3) and co-treated with varying
782 doses of ISRIB. IC50 (95% Confidence Interval) was calculated and indicated at the top of each
783 graph. **I.** Immunoblot showing the levels of the indicated proteins in MDA-MB-436 and Hs 578T
784 cells exposed to DMSO (0.2%), UNC1999 and EPZ-6438 (1μM; 72 h; N=3) and treated with the
785 integrated stress response inhibitor (ISRIB; 100nM; vs DMSO). **J.** Quantification of the relative
786 protein levels from Fig. 2H (rel. to Lamin B1; N=3). Data are the mean ± SD from 3 biological
787 replicates (B, D, E, G, H and J). Statistical analysis performed using one-way (D and J) and two-
788 way ANOVA (B, E and G). ns, not significant, *$p < 0.05$, **$p < 0.01$, ***$p < 0.001$, ****$p <$
789 0.0001. R: replicate #.

FIGURE 3

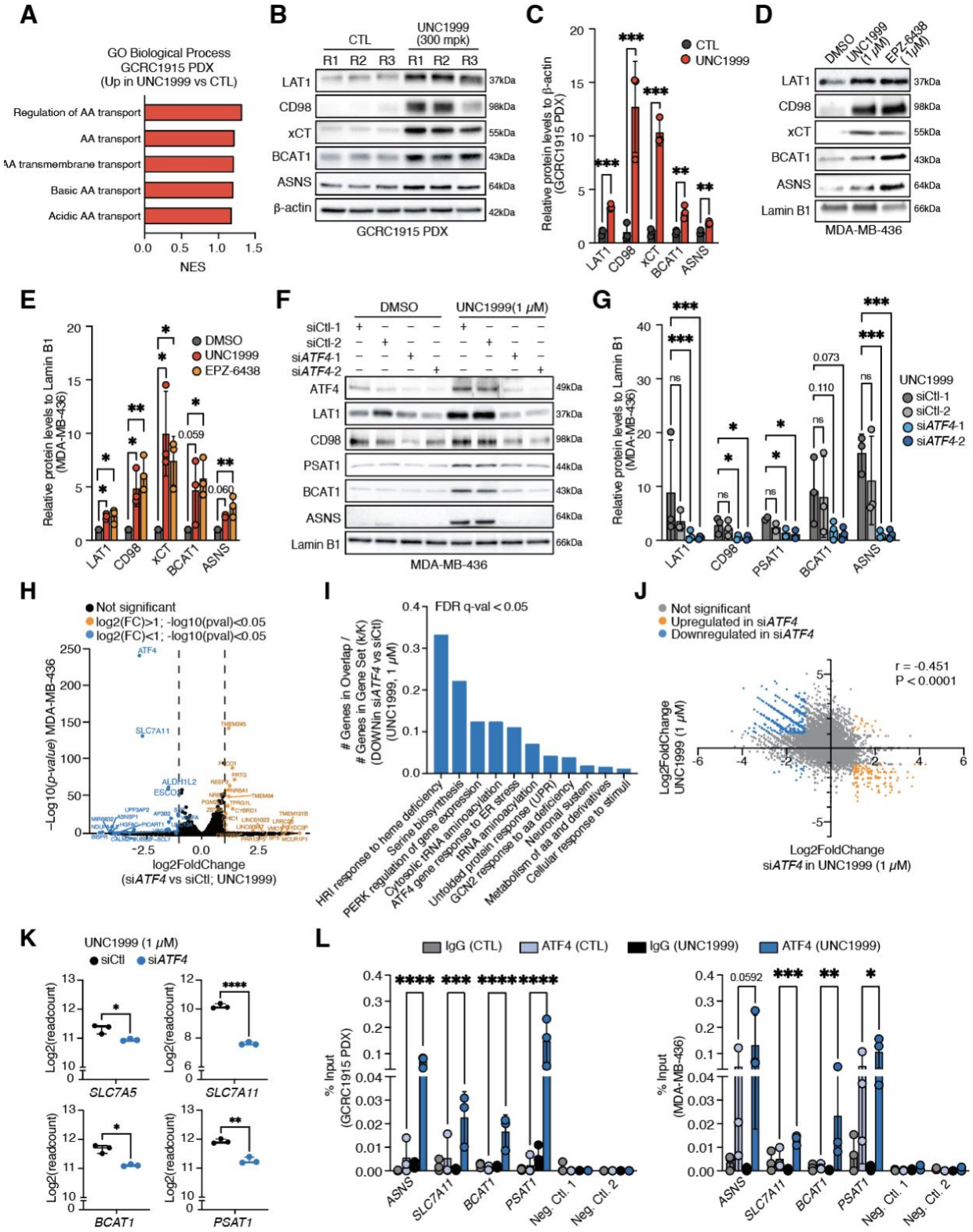
A
GO Biological Process
GCRC1915 PDX
(Up in UNC1999 vs CTL)
Regulation of AA transport
AA transport
AA transmembrane transport
Basic AA transport
Acidic AA transport
NES
B
CTL
UNC1999 (300 mpk)
R1 R2 R3 R1 R2 R3
LAT1
CD98
xCT
BCAT1
ASNS
β-actin
GCRC1915 PDX
C
CTL
UNC1999
Relative protein levels to β-actin (GCRC1915 PDX)
D
DMSO
UNC1999 (1 μM)
EPZ-6438 (1 μM)
Lamin B1
MDA-MB-436
E
DMSO
UNC1999
EPZ-6438
Relative protein levels to Lamin B1 (MDA-MB-436)
F
DMSO
UNC1999(1 μM)
siCtl-1
siCtl-2
siATF4-1
siATF4-2
ATF4
PSAT1
MDA-MB-436
G
UNC1999
siCtl-1
siCtl-2
siATF4-1
siATF4-2
H
Not significant
log2(FC)>1; -log10(pval)<0.05
log2(FC)<1; -log10(pval)<0.05
−Log10(p-value) MDA-MB-436
log2FoldChange
(siATF4 vs siCtl; UNC1999)
I
FDR q-val < 0.05
Genes in Overlap / # Genes in Gene Set (k/K)
(DOWNin siATF4 vs siCtl) (UNC1999, 1 μM)
HRI response to heme deficiency
Serine biosynthesis
PERK regulation of gene expression
Cytosolic tRNA aminoacylation
ATF4 gene response to ER stress
tRNA aminoacylation
Unfolded protein response (UPR)
GCN2 response to aa deficiency
Neuronal system
Metabolism of aa and derivatives
Cellular response to stimuli
J
Not significant
Upregulated in siATF4
Downregulated in siATF4
r = -0.451
P < 0.0001
Log2FoldChange UNC1999 (1 μM)
Log2FoldChange
siATF4 in UNC1999 (1 μM)
K
UNC1999 (1 μM)
siCtl
siATF4
Log2(readcount)
SLC7A5
SLC7A11
BCAT1
PSAT1
L
IgG (CTL)
ATF4 (CTL)
IgG (UNC1999)
ATF4 (UNC1999)
% Input (GCRC1915 PDX)
% Input (MDA-MB-436)
ASNS
SLC7A11
BCAT1
PSAT1
Neg. Ctl. 1
Neg. Ctl. 2

792 **Figure 3.** ATF4 Regulates an Amino Acid Gene Signature in Response to EZH2 Inhibition in
793 TNBC. **A.** GSEA bar graph displaying significantly enriched metabolism-related gene ontology
794 biological process (GOBP) pathways ($p<0.05$), from genes significantly up-regulated in
795 UNC1999-treated GCRC1915-PDX (300 mg/kg; 21 days) relative to control (N=3). **B.**
796 Immunoblot showing LAT1, CD98, xCT, BCAT1, ASNS and β-actin levels in GCRC1915 PDX
797 exposed to control or UNC1999 (300 mg/kg; 21 days; N=3). **C.** Quantification of the relative
798 protein levels from Fig. 3B (rel. to β-actin; N=3). **D.** Same as in B in MDA-MB436 cells exposed
799 to DMSO (0.2%) or UNC1999 (1μM; 96 h; N=3). **E.** Quantification of the relative protein levels
800 from Fig. 3D (rel. to Lamin B1; N=3). **F.** Immunoblot showing the levels of ATF4, LAT1, CD98,
801 PSAT1, BCAT1, ASNS and Lamin B1 in MDA-MB-436 cells exposed to DMSO (0.2%) or
802 UNC1999 (1μM; 72 h; N=3) and depleted for ATF4 using two siRNAs against *ATF4* (72 h) vs
803 non-targeting siRNA (siCtl). **G.** Quantification of the relative protein levels from Fig. 3F (rel. to
804 Lamin B1; N=3). **H.** Volcano plots showing the -Log10(*p-value*) and the Log2 fold change in gene
805 expression upon ATF4 depletion by siRNA (48 h) in MDA-MB-436 cells exposed to UNC1999
806 (1μM, 48 h, N=3). **I.** Bar graph representing up-regulated pathways (GSEA) following ATF4
807 depletion in MDA-MB-436 cells exposed to UNC1999 (1μM; 48 h; N=3) vs DMSO (0.2%). **J.**
808 Scatter plot representation of Log2 fold change in gene expression resulting from UNC1999 vs
809 DMSO (vertical) and si*ATF4* vs siCtl in UNC1999-treated MDA-MB-436 cells (1μM; 48 h; N=3)
810 ($r= -0.451$; p-value<0.0001). **K.** Gene expression levels of *SLC5A7*, *SLC7A11*, *PSAT1,* and *BCAT1*
811 upon depletion of ATF4 (siATF4) vs siCtl in MDA-MB-436 cells exposed to UNC1999 (1μM; 48
812 h; N=3). **L.** ATF4 Chromatin immunoprecipitation followed by qPCR amplification at specific
813 ATF4 target gene promoters (*ASNS*, *SLC7A11*, *BCAT1,* and *PSAT1*) in none-treated vs UNC1999-
814 treated GCRC1915 PDX (left; 300 mg/kg; 21 days; N=3) and MDA-MB-436 (right; 1μM; 48 h).
815 Data are shown as %input. The data presented are the mean ± SD from 3 biological replicates (C,
816 E, G, K and L). Statistical analysis was performed using one-way ANOVA (E, G and L) and two-
817 tailed Student's t test (C and K). ns, not significant, *$p < 0.05$, **$p < 0.01$, ***$p < 0.001$, ****$p <$
818 0.0001. R: replicate #.

FIGURE 4

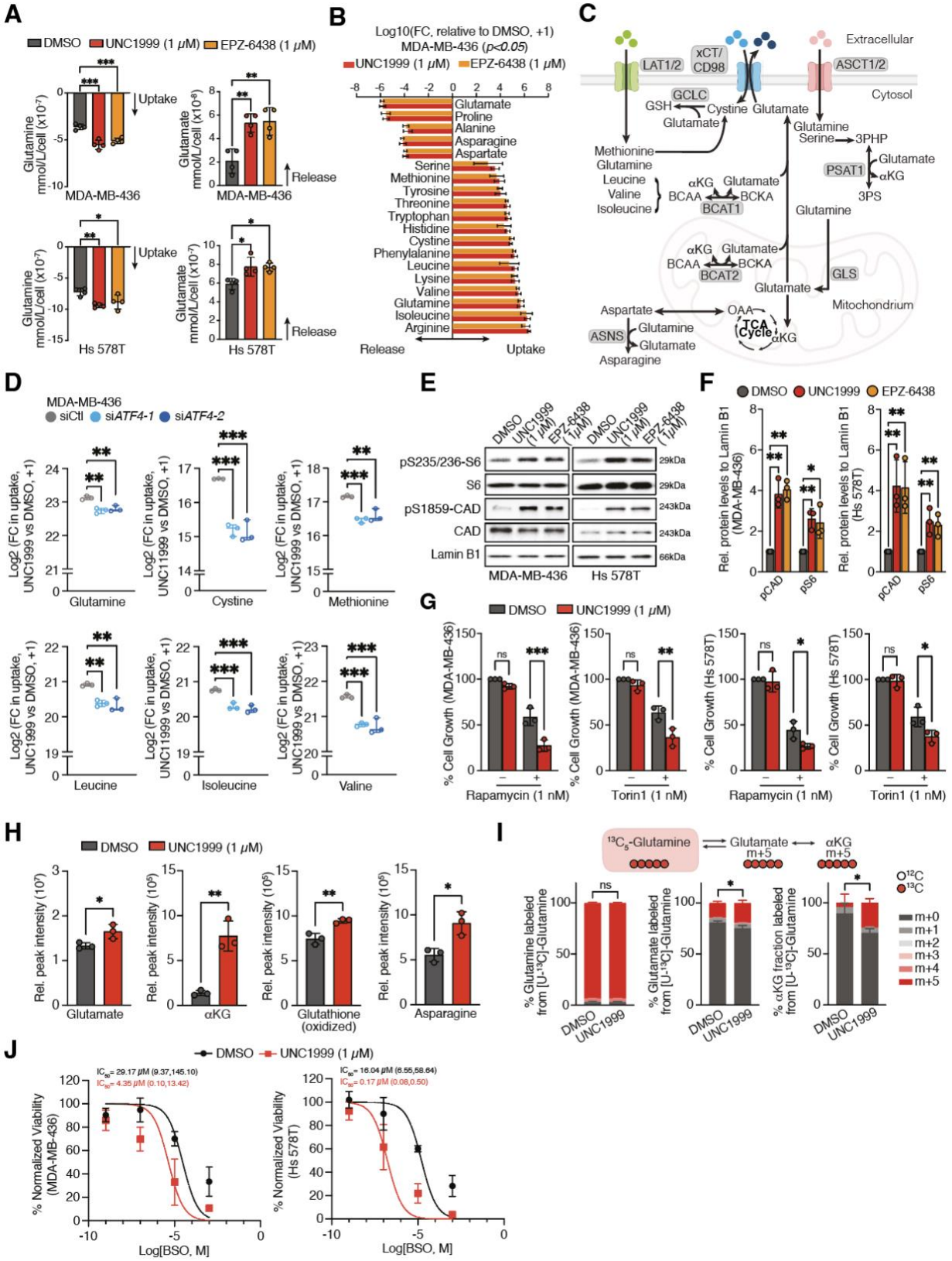
A
DMSO
UNC1999 (1 μM)
EPZ-6438 (1 μM)
Glutamine mmol/L/cell (x10⁻⁷)
Uptake
Glutamate mmol/L/cell (x10⁻⁸)
Release
MDA-MB-436
Hs 578T
B
Log10(FC, relative to DMSO, +1)
MDA-MB-436 (p<0.05)
UNC1999 (1 μM)
EPZ-6438 (1 μM)
Glutamate
Proline
Alanine
Asparagine
Aspartate
Serine
Methionine
Tyrosine
Threonine
Tryptophan
Histidine
Cystine
Phenylalanine
Leucine
Lysine
Valine
Glutamine
Isoleucine
Arginine
Release
Uptake
C
Extracellular
LAT1/2
xCT/ CD98
ASCT1/2
Cytosol
GCLC
GSH
Cystine
Glutamate
Glutamine
Serine
3PHP
Methionine
Glutamine
Leucine
Valine
Isoleucine
αKG
BCAA
BCKA
BCAT1
PSAT1
3PS
BCAT2
GLS
Mitochondrium
Aspartate
OAA
TCA Cycle
ASNS
Asparagine
D
MDA-MB-436
siCtl
siATF4-1
siATF4-2
Log2 (FC in uptake, UNC1999 vs DMSO, +1)
Log2 (FC in uptake, UNC11999 vs DMSO, +1)
Glutamine
Cystine
Methionine
Leucine
Isoleucine
Valine
E
DMSO
UNC1999 (1 μM)
EPZ-6438 (1 μM)
pS235/236-S6
S6
pS1859-CAD
CAD
Lamin B1
29kDa
243kDa
66kDa
MDA-MB-436
Hs 578T
F
DMSO
UNC1999
EPZ-6438
Rel. protein levels to Lamin B1 (MDA-MB-436)
Rel. protein levels to Lamin B1 (Hs 578T)
pCAD
pS6
G
DMSO
UNC1999 (1 μM)
% Cell Growth (MDA-MB-436)
% Cell Growth (Hs 578T)
Rapamycin (1 nM)
Torin1 (1 nM)
ns
H
DMSO
UNC1999 (1 μM)
Rel. peak intensity (10⁷)
Rel. peak intensity (10⁶)
Rel. peak intensity (10⁵)
Glutamate
αKG
Glutathione (oxidized)
Asparagine
I
¹³C₅-Glutamine
Glutamate m+5
αKG m+5
¹²C
¹³C
% Glutamine labeled from [U-¹³C]-Glutamine
% Glutamate labeled from [U-¹³C]-Glutamine
% αKG fraction labeled from [U-¹³C]-Glutamine
m+0
m+1
m+2
m+3
m+4
m+5
DMSO
UNC1999
J
DMSO
UNC1999 (1 μM)
IC50= 29.17 μM (9.37,145.10)
IC50= 4.35 μM (0.10,13.42)
IC50= 16.04 μM (6.55,58.64)
IC50= 0.17 μM (0.08,0.50)
% Normalized Viability (MDA-MB-436)
% Normalized Viability (Hs 578T)
Log[BSO, M]

819

820 **Figure 4.** EZH2 Inhibition Induces ATF4-Mediated Metabolic Adaptation in TNBC. **A.** Relative
821 quantification of glutamine and glutamate (BioProfile 400, Nova Biomedical) in conditioned
822 media exposed to MDA-MB-436 or Hs 578T cells treated with UNC1999 or EPZ-6438 (1μM; 72
823 h) or DMSO (0.2%; N=4). **B.** Relative metabolite quantification in conditioned media using Triple
824 Quadrupole-Liquid Chromatography-Mass Spectrometry (QQQ-LC-MS; Intrada-amino-acids) in
825 MDA-MB-436 cells exposed to UNC1999 or EPZ-6438 ($p<0.05$; 1μM; 72 h) or DMSO (0.2%;
826 N=4). Metabolite levels for each experimental condition are normalized to those of the naïve
827 medium. **C.** Schematic representation of amino acid uptake and glutaminolysis coupled with
828 transaminase reactions and antioxidant response. **D.** Relative metabolite levels in conditioned
829 media using QQQ-LC-MS (Intrada-amino-acids) in MDA-MB-436 cells exposed to DMSO
830 (0.2%) or UNC1999 (1μM; 60h) and transfected with non-targeting siRNA (siCtl) or two siRNA
831 against *ATF4* (20nM; 60h; N=3). Metabolite levels for each experimental condition are normalized
832 against those of the naïve medium. **E.** Immunoblot showing pS1859-CAD, CAD, pS235/236-S6,
833 S6 and Lamin B1 levels in MDA-MB-436 or Hs 578T cells exposed to UNC1999, EPZ-6438
834 (1μM; 96 h) or DMSO (0.2%; N=3). **F.** Quantification of the relative protein levels from Fig. 4D
835 (rel. to Lamin B1; N=3). **G.** Percent growth of MDA-MB-436 and Hs 578T cells exposed to
836 UNC1999 (1μM; 96 h) or DMSO (0.2%; N=3) exposed to DMSO (0.1%), Rapamycin (1nM) or
837 Torin1 (1nM). **H.** Quantification of selected intracellular metabolites in Hs 578T cells using
838 Quadrupole Time-of-Flight (QTOF)-LC-MS (Ion-pairing) exposed to UNC1999 (1μM; 72 h) or
839 DMSO (0.2%; N=3). **I.** Stack bars illustrating stable isotope tracing analysis (SITA) using
840 glutamine-deprived media supplemented with $^{13}C_5$-glutamine (4mM) to identify the fractional
841 pool of labeled glutaminolysis intermediates (glutamine m+5, glutamate m+5 and αKG m+5) in
842 Hs 578T cells exposed to DMSO (0.2%) or UNC1999 (1μM, 96 h), quantified by QTOF-LC-MS
843 (ion pairing) after 30 minutes exposure to $^{13}C_5$-glutamine. **J.** Dose-response curves representing
844 the relative normalized viability of MDA-MB-436 (left) and Hs 578T (right) cells exposed to
845 DMSO (0.2%) or UNC1999 (1μM; 96h; N=3) and co-treated with varying doses of L-Buthionine
846 sulfoximine (BSO), a potent inhibitor of the catalytic subunit of glutamate-cysteine ligase (GCLC).
847 IC50 (95% Confidence Interval) was calculated and indicated at the top of each graph. The data
848 shown are the mean ± SD from 3 to 4 biological replicates (A, B, D, F, G, H, I and J). Statistical
849 analysis was performed by one-way (A, D and F) and two-way ANOVA (G), and two-tailed
850 Student's t test (H and I). ns, not significant, *$p < 0.05$, **$p < 0.01$, ***$p < 0.001$.

FIGURE 5

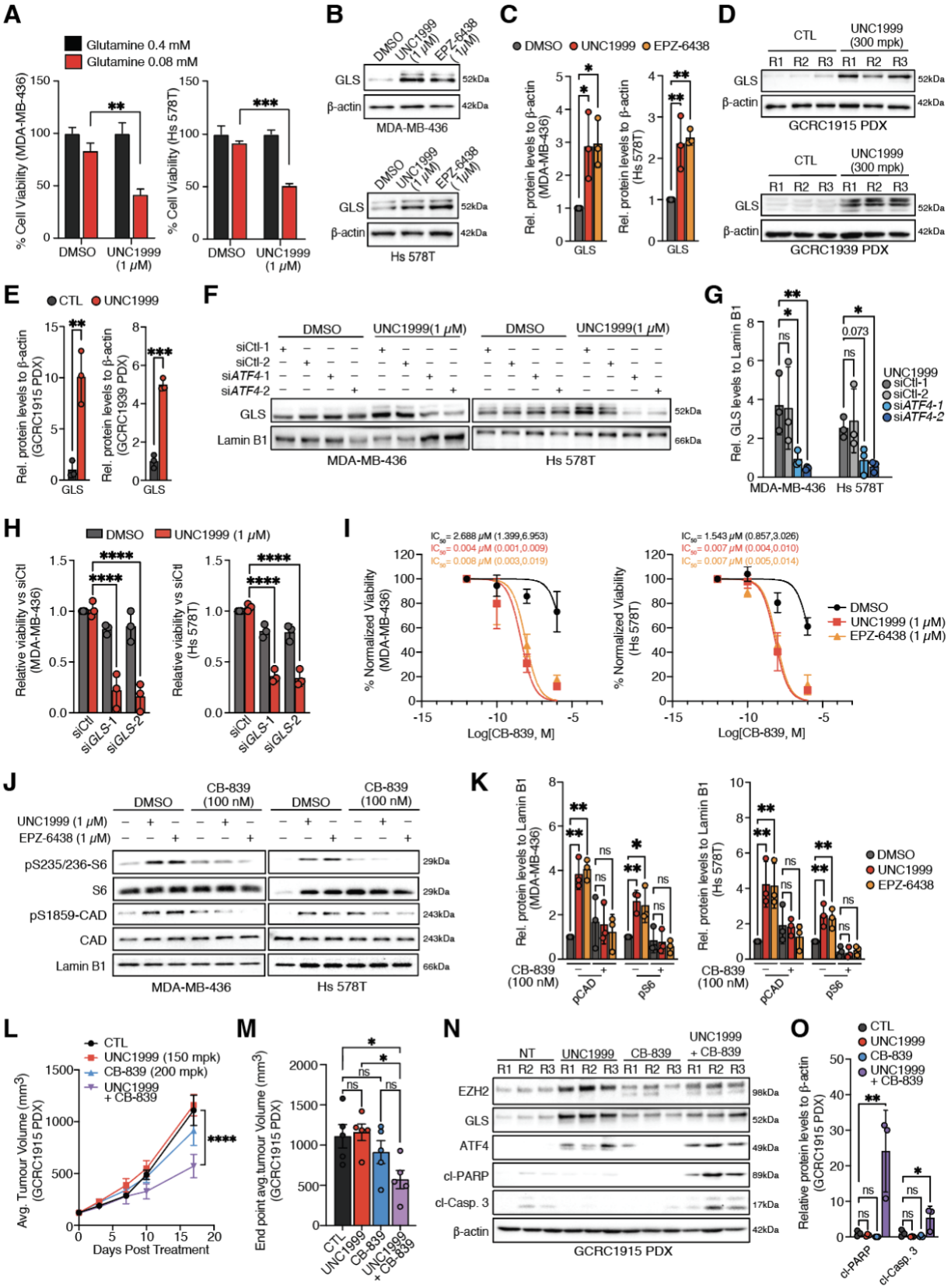
A
Glutamine 0.4 mM
Glutamine 0.08 mM
% Cell Viability (MDA-MB-436)
% Cell Viability (Hs 578T)
DMSO
UNC1999 (1 μM)
B
DMSO
UNC1999 (1 μM)
EPZ-6438 (1 μM)
GLS
β-actin
52kDa
42kDa
MDA-MB-436
Hs 578T
C
DMSO
UNC1999
EPZ-6438
Rel. protein levels to β-actin (MDA-MB-436)
Rel. protein levels to β-actin (Hs 578T)
GLS
D
CTL
UNC1999 (300 mpk)
R1 R2 R3 R1 R2 R3
GCRC1915 PDX
GCRC1939 PDX
E
CTL
UNC1999
Rel. protein levels to β-actin (GCRC1915 PDX)
Rel. protein levels to β-actin (GCRC1939 PDX)
F
DMSO
UNC1999(1 μM)
siCtl-1
siCtl-2
siATF4-1
siATF4-2
Lamin B1
66kDa
G
Rel. GLS levels to Lamin B1
0.073
ns
UNC1999
siCtl-1
siCtl-2
siATF4-1
siATF4-2
H
DMSO
UNC1999 (1 μM)
Relative viability vs siCtl (MDA-MB-436)
Relative viability vs siCtl (Hs 578T)
siCtl
siGLS-1
siGLS-2
I
IC50= 2.688 μM (1.399,6.953)
IC50= 0.004 μM (0.001,0.009)
IC50= 0.008 μM (0.003,0.019)
IC50= 1.543 μM (0.857,3.026)
IC50= 0.007 μM (0.004,0.010)
IC50= 0.007 μM (0.005,0.014)
% Normalized Viability (MDA-MB-436)
% Normalized Viability (Hs 578T)
Log[CB-839, M]
DMSO
UNC1999 (1 μM)
EPZ-6438 (1 μM)
J
DMSO
CB-839 (100 nM)
UNC1999 (1 μM)
EPZ-6438 (1 μM)
pS235/236-S6
S6
pS1859-CAD
CAD
Lamin B1
29kDa
243kDa
66kDa
K
Rel. protein levels to Lamin B1 (MDA-MB-436)
Rel. protein levels to Lamin B1 (Hs 578T)
CB-839 (100 nM)
pCAD
pS6
DMSO
UNC1999
EPZ-6438
L
CTL
UNC1999 (150 mpk)
CB-839 (200 mpk)
UNC1999 + CB-839
Avg. Tumour Volume (mm3) (GCRC1915 PDX)
Days Post Treatment
M
End point avg.tumour Volume (mm3) (GCRC1915 PDX)
CTL
UNC1999
CB-839
UNC1999 + CB-839
N
NT
UNC1999
CB-839
UNC1999 + CB-839
R1 R2 R3 R1 R2 R3 R1 R2 R3 R1 R2 R3
EZH2
GLS
ATF4
cl-PARP
cl-Casp. 3
β-actin
98kDa
52kDa
49kDa
89kDa
17kDa
42kDa
GCRC1915 PDX
O
CTL
UNC1999
CB-839
UNC1999 + CB-839
Relative protein levels to β-actin (GCRC1915 PDX)
cl-PARP
cl-Casp. 3

851

852 **Figure 5.** Blocking glutaminase sensitizes TNBC to EZH2 inhibition. **A.** Percent viability of
853 MDA-MB-436 (left) or Hs 578T (right) cells exposed to UNC1999 (1μM; 96 h) or DMSO (0.2%;
854 N=3) exposed to either full media (0.4 mM glutamine) or to media depleted in glutamine (0.08
855 mM) (data shown relative to full media). **B.** Immunoblot showing GLS and β-actin levels in
856 MDA-MB-436 or Hs 578T cells exposed to UNC1999, EPZ-6438 (1μM; 96 h) or DMSO (0.2%;
857 N=3). **C.** Quantification of the relative GLS levels from Fig. 5B (rel. to β-actin; N=3). **D.**
858 Immunoblot showing GLS and β-actin levels in GCRC1915 and GCRC1939 PDXs exposed or not
859 to UNC1999 (300 mg/kg; 21 days; N=3). **E.** Quantification of the relative GLS levels from Fig.
860 5D (rel. to β-actin; N=3). **F.** Immunoblot showing GLS and Lamin B1 levels in MDA-MB-436
861 or Hs 578T cells exposed to UNC1999 (1μM; 72 h) or DMSO (0.2%; N=3) and depleted of ATF4
862 using two siRNAs against *ATF4* (60h) vs non-targeting siRNAs (siCtl). **G.** Quantification of the
863 relative GLS levels from Fig. 5F (rel. to Lamin B1; N=3). **H.** Relative viability (crystal violet) of
864 MDA-MB-436 and Hs 578T cells depleted of GLS using siRNAs (vs siCtl) and exposed to
865 UNC1999 (1μM; 96 h) or DMSO (0.2%; N=3). **I.** Dose-response curves representing the relative
866 normalized viability of MDA-MB-436 (left) and Hs 578T (right) cells exposed to DMSO (0.2%),
867 UNC1999 or EPZ-6438 (1μM; 120h) (N=3) and co-treated with varying doses of CB-839. IC50
868 (95% Confidence Interval) was calculated and indicated at the top of each graph. **J.** Immunoblot
869 showing pS1859-CAD, CAD, pS235/236-S6, S6 and Lamin B1 levels in MDA-MB-436 or Hs
870 578T cells treated with DMSO (0.2%), UNC1999 or EPZ-6438 (1μM; 96 h; N=3) and exposed to
871 CB-839 (100nM). **K.** Quantification of the relative protein levels from Fig. 5J (rel. to Lamin B1;
872 N=3). **L.** Graph showing average tumor volume over time for GCRC1915 PDX implanted in
873 female NSG mice and treated as indicated (control, CB-839 (200 mg/kg; 17 days), UNC1999 (150
874 mg/kg; 17 days) or combination) (17 days; N=5 per group). **M.** Bar graph showing average tumor
875 volume as in J on day 17 (endpoint). **N.** Immunoblot showing EZH2, GLS, ATF4, cl-PARP, cl-
876 Caspase3, and β-actin levels in GCRC1915 PDX tumors treated with CTL, CB-839 (200 mg/kg),
877 UNC1999 (150 mg/kg), or combination (17 days; N=3). **O.** Quantification of the relative cl-PARP
878 and cl-caspase3 levels from Fig. 5N (rel. to β-actin; N=3). Data represented are means ± SD from
879 3 biological replicates (A, C, E, G, H, I, K and O); error bars represent SEM for tumor volume (L
880 and M). Statistical analysis was performed by one-way (C, G, K, M and O) and two-way ANOVA
881 (H and L) and two-tailed Student's t test (A and E). ns, not significant, *$p < 0.05$, **$p < 0.01$, ***p
882 < 0.001, ****$p < 0.0001$. R: replicate #.

FIGURE S1

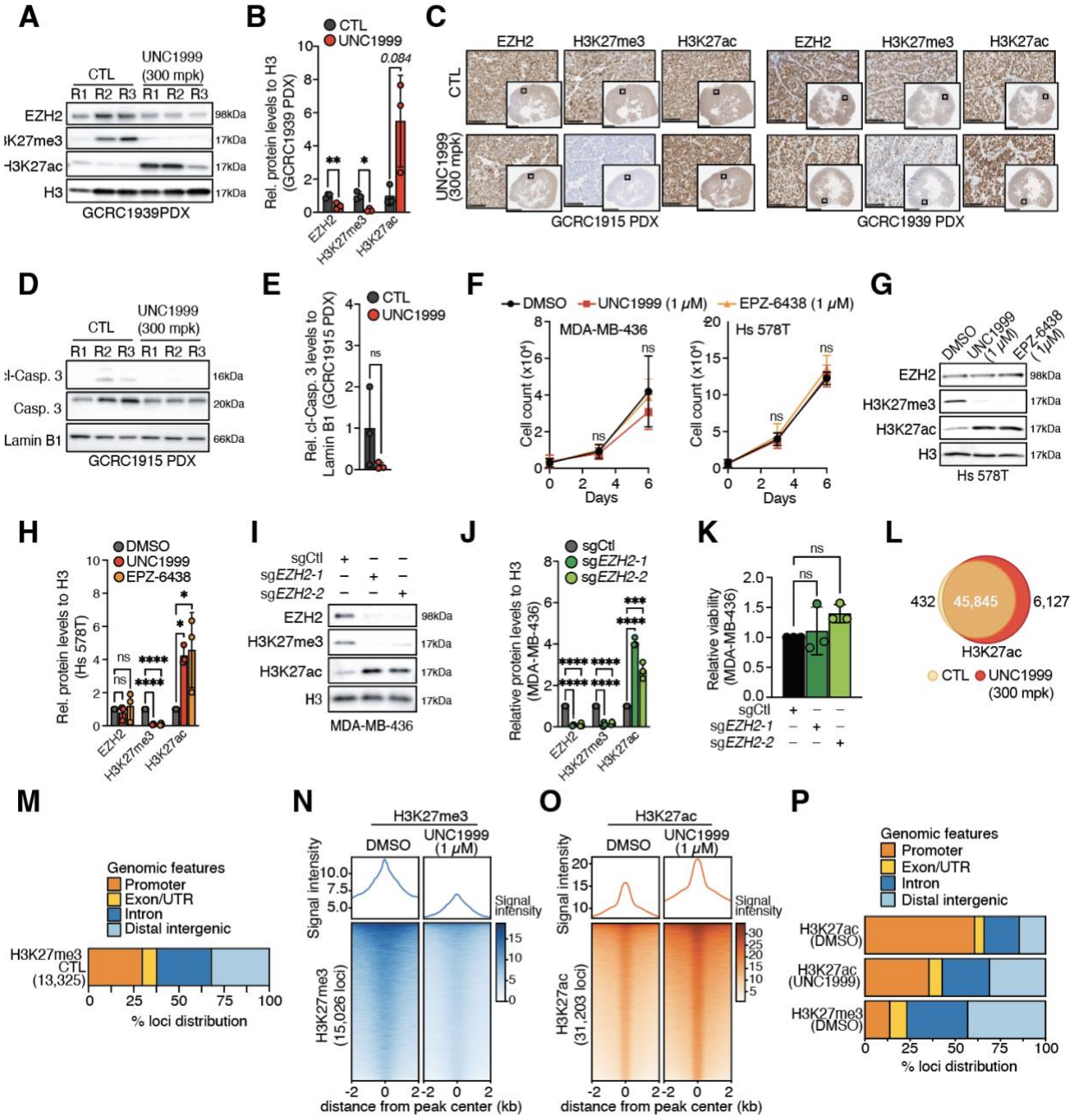

883

884

885 **Supplementary Figure 1. A.** Immunoblot showing the levels of EZH2, H3K27me3, H3K27ac,
886 and total H3 in GCRC1939 PDX exposed or not to UNC1999 (300 mg/kg; 21 days; N=3). **B.**
887 Quantification of the relative protein levels from Fig.S1A (rel. to H3; N=3). **C.**
888 Immunohistochemistry staining of EZH2, H3K27me3, and H3K27ac on GCRC1915 and
889 GCRC1939 PDX exposed or not to UNC1999 (300 mg/kg, 21 days) (N=3); magnification, 20X;
890 scale bars, 100µm. **D.** Immunoblot showing cl-Caspase 3, Caspase 3 and Lamin B1 levels in
891 GCRC1915-PDX exposed or not to UNC1999 (300 mg/kg; 21 days) (N=3). **E.** Quantification of
892 the relative cl-Caspase 3 levels from Fig.S1D (rel. to Lamin B1; N=3). **F.** Cell counts representing
893 cell proliferation of MDA-MB-436 (left) and Hs 578T (right) cells exposed to UNC1999 or EPZ-
894 6438 (1µM) or DMSO (0.2%) for up to 6 days (N=3). **G.** Immunoblot showing EZH2, H3K27me3,
895 H3K27ac, and total H3 levels in Hs 578T cells exposed to UNC1999, EPZ-6438 (1 µM, 96 h;
896 N=3) or mock treated (DMSO, 0.2%). **H.** Quantification of the relative protein levels from Fig.S1G
897 (rel. to H3; N=3). **I.** Immunoblot showing EZH2, H3K27me3, H3K27ac, and total H3 levels in
898 MDA-MB436-EZH2 knock-out cells using two sgRNAs targeting EZH2 or non-targeting sgRNA
899 (sgCtl) (N=3). **J.** Quantification of the relative protein levels from Fig.S1I (rel. to H3; N=3). **K.**
900 Relative viability (crystal violet) of MDA-MB-436 EZH2 knock-out cells using two different
901 sgRNAs against *EZH2* (120h) or sgCtl (N=3). **L.** Venn diagrams representing the number of
902 H3K27ac peaks that are common, specific to control, or to UNC1999 treatment (300 mg/kg, 21
903 days) in GCRC1915-PDX (N=2-3). **M.** Stacked bar charts illustrating the proportion of
904 H3K27me3 peaks associated with distinct genomic localization/features relative to gene TSS upon
905 control treatment in GCRC1915 PDX (300 mg/kg, 21 days; N=2-3). **N.** Heatmap of peak intensity
906 signal of H3K27me3 ChIP-seq peaks (–2 to +2kbp window from peak center) in MDA-MB-436
907 cells treated with DMSO (0.2%; left) or UNC1999 (1µM; right) (N=3). Compiled tag density plots
908 are illustrated at the top of each condition. **O.** Heatmap of peak intensity signal of H3K27ac upon
909 DMSO (0.2%; left) or UNC1999 (1µM; right) treatment in MDA-MB-436 cells (N=2). Compiled
910 tag density plots are illustrated at the top of each condition. **P.** Bar charts illustrating the proportion
911 of H3K27me3 and H3K27ac peaks following DMSO (0.2%) or UNC1999 treatment (1µM; 96 h)
912 in MDA-MB436 cells and associated with genomic features relative to gene TSS (N=2-3). Data
913 represent the mean ± SD from 3 biological replicates (B, E, G, H, J and K). Statistical analysis was
914 performed by two-tailed Student's t test (B and E), one-way (G, J and K) and two-way ANOVA
915 (H). ns, not significant, *$p < 0.05$, **$p < 0.01$, ***$p < 0.001$, ****$p < 0.0001$. R: replicate #.

FIGURE S2

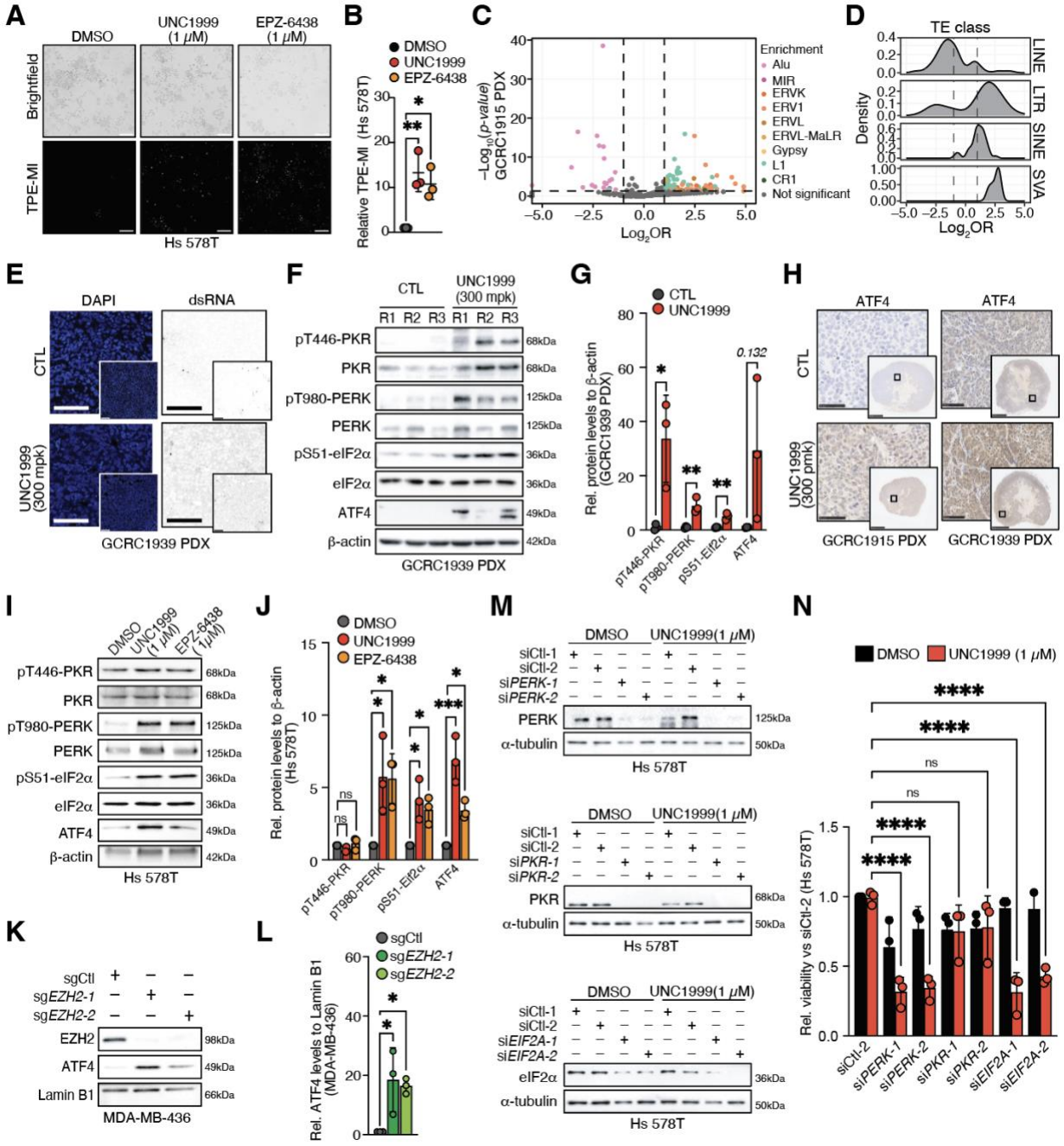

916

917 **Supplementary Figure 2. A.** Detection of unfolded protein load in Hs 578T cells exposed to
918 UNC1999 or EPZ-6438 (1μM; 48 h) or DMSO (0.2%; N=3), using the tetraphenyl ethene
919 maleimide (TPE-MI) probe (IF) detecting misfolded protein loads. Cell density is shown in
920 brightfield. Scale bar, 100μm. **B.** Quantification of misfolded protein load from Fig.S2A showing
921 TPE-MI intensity normalized to naïve media and relative to DMSO (0.2%). **C.** Volcano plot
922 showing enrichment level of significantly upregulated transposable elements (TE) insertions in
923 UNC1999-treated GCRC1915 PDX (300 mg/kg; 21 days; N=3) relative to control. Colors
924 correspond to their associated families. Odds ratio (OR) and p-value computed using Fisher's exact
925 test. **D.** Density chart representing global enrichment of TEs fully located within H3K27me3 peaks
926 that gained H3K27ac following UNC1999 treatment in GCRC1915 PDX (N=2-3). Odds ratio
927 (OR) and p-value computed using Fisher's exact test. **E.** Immunofluorescence staining using J2
928 antibody in GCRC1939 PDX exposed to UNC1999 (300 mg/kg; 21 days) or control (N=3). Scale
929 bar, 100μm. **F.** Immunoblot showing the levels of pT980-PERK, PERK, pT446-PKR, PKR, pS51-
930 eIF2α, eIF2α, ATF4 and β-actin in GCRC1939-PDX exposed to UNC1999 (300 mg/kg; 21 days)
931 or Control (N=3). **G.** Quantification of the relative protein levels from Fig. S2E (rel. to β-actin;
932 N=3). **H.** IHC staining of ATF4 on GCRC1915 and GCRC1939 PDX exposed to UNC1999 (300
933 mg/kg, 21 weeks) or control (N=3). **I.** Immunoblot showing pT446-PKR, PKR, pT980-PERK,
934 PERK, pS51-eIF2α, eIF2α, ATF4 and β-actin levels in Hs 578T exposed to control or UNC1999
935 (300 mg/kg; 21 days; N=3). **J.** Quantification of the relative protein levels from Fig.S2H (rel. to
936 β-actin; N=3). **K.** Immunoblot showing EZH2, ATF4 and Lamin B1 levels in MDA-MB-436
937 EZH2 knock-out cells using two different sgRNAs (N=3). **L.** Quantification of the relative protein
938 levels from Fig.S2J (rel. to Lamin B1; N=3). **M.** Immunoblot showing the levels of the indicated
939 proteins (PKR, PERK, eIF2α , and α-tubulin) in Hs 578T cells exposed to UNC1999 (1μM; 48 h)
940 or DMSO (0.2%; N=3) and depleted or not for the indicated gene/protein using two siRNAs/gene.
941 **N.** Relative viability (crystal violet) of Hs 578T cells depleted of either PKR, PERK, or eIF2α
942 using siRNAs (72 h) or siCtl and exposed to EZH2 inhibitor UNC1999 (1μM; 96 h) or DMSO
943 (0.2%; N=3). Data shown are the mean ± SD from 3 biological replicates (B, G, J, L and N).
944 Statistical analysis was performed by two-tailed Student's t test (G), one-way (B, J and L) and
945 two-way ANOVA (N). ns, not significant, *$p < 0.05$, **$p < 0.01$, ***$p < 0.001$, ****$p < 0.0001$.
946 R: replicate #.

FIGURE S3

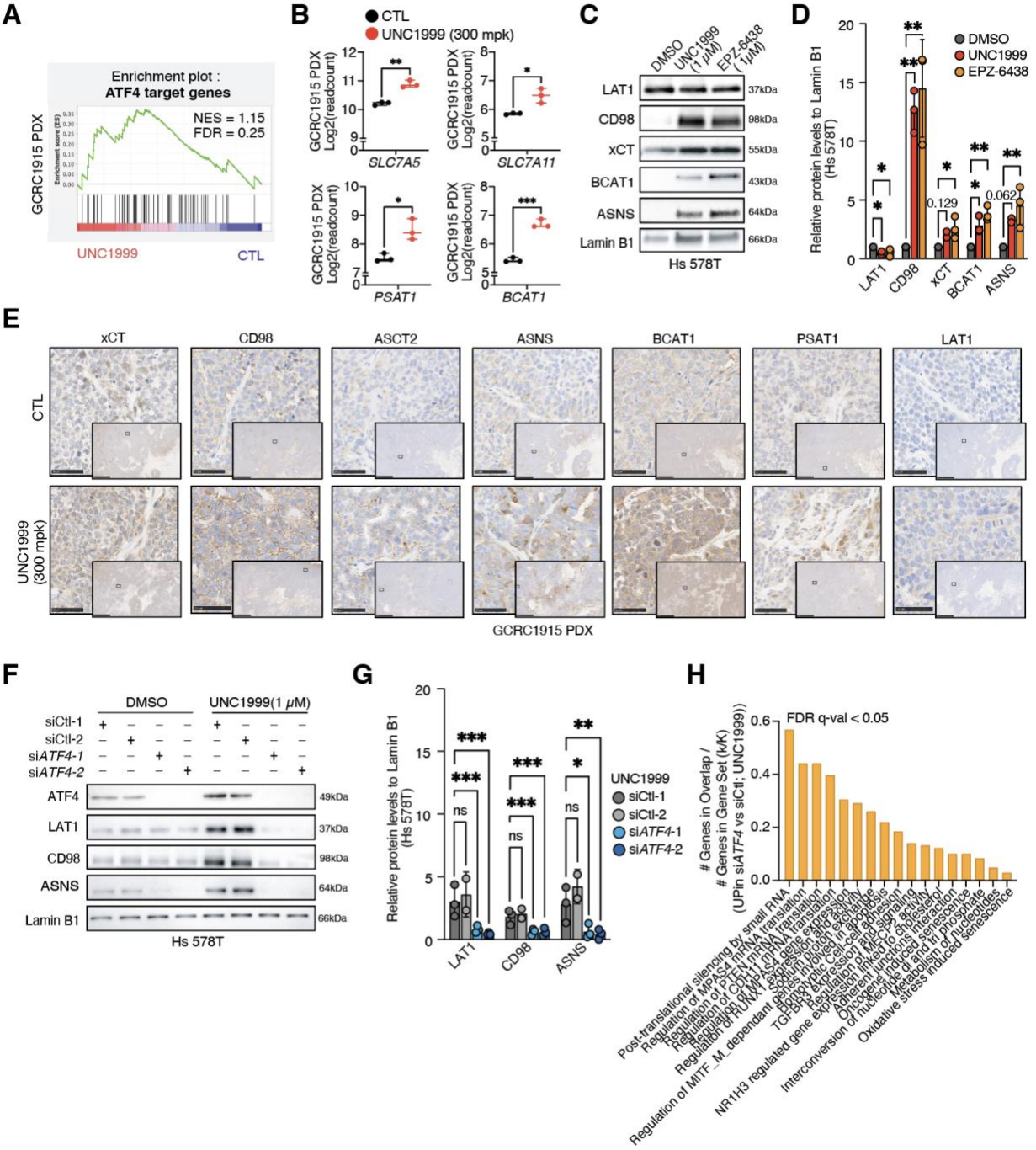

947

948 **Supplementary Figure 3. A.** GSEA plot showing NES for *ATF4 targets* gene set generated from
949 Koumenis et al.[60] in GCRC1915 PDX exposed to UNC1999 (300 mg/kg, 21 days) or CTL (N=3).
950 **B.** Gene expression levels of *SLC5A7*, *SLC7A11*, *PSAT1* and *BCAT1* in GCRC1915 PDX exposed
951 to UNC1999 (300 mg/kg; 21 days) relative to control (N=3). **C.** Immunoblot showing LAT1,
952 CD98, xCT, BCAT1, ASNS and Lamin B1 levels in Hs 578T exposed to DMSO (0.2%) or
953 UNC1999 (1µM; 96 h; N=3). **D.** Quantification of the relative protein levels from Fig. S3C (rel.
954 to Lamin B1; N=3). **E.** Immunohistochemistry staining of LAT1, CD98, xCT, ASCT2, PSAT1,
955 BCAT1 and ASNS in GCRC1915 PDX exposed or not to UNC1999 (300 mg/kg; 21 days; N=3).
956 Magnification, 2.5X and 40X. Scale bars, 50µm. **F.** Immunoblot showing the levels of ATF4,
957 LAT1, CD98, ASNS and Lamin B1 in Hs 578T cells exposed to DMSO (0.2%) or UNC1999
958 (1µM; 72 h) (N=3) and depleted for ATF4 using 2 siRNAs (72 h). **G.** Quantification of the relative
959 protein levels from Fig. S3F (rel. to Lamin B1; N=3). **H.** Bar graph representing down-regulated
960 pathways (Reactome gene set) following ATF4 depletion in MDA-MB-436 cells exposed to
961 UNC1999 (1µM; 48 h) relative to DMSO (0.2%; N=3). Data analysis is presented as the mean ±
962 SD from three biological replicates (B, D and G). Statistical analysis was performed by two-tailed
963 Student's t test (B) and one-way ANOVA (D and G). ns, not significant, *$p < 0.05$ **$p < 0.01$,
964 ***$p < 0.001$. R: replicate #.
965

FIGURE S4

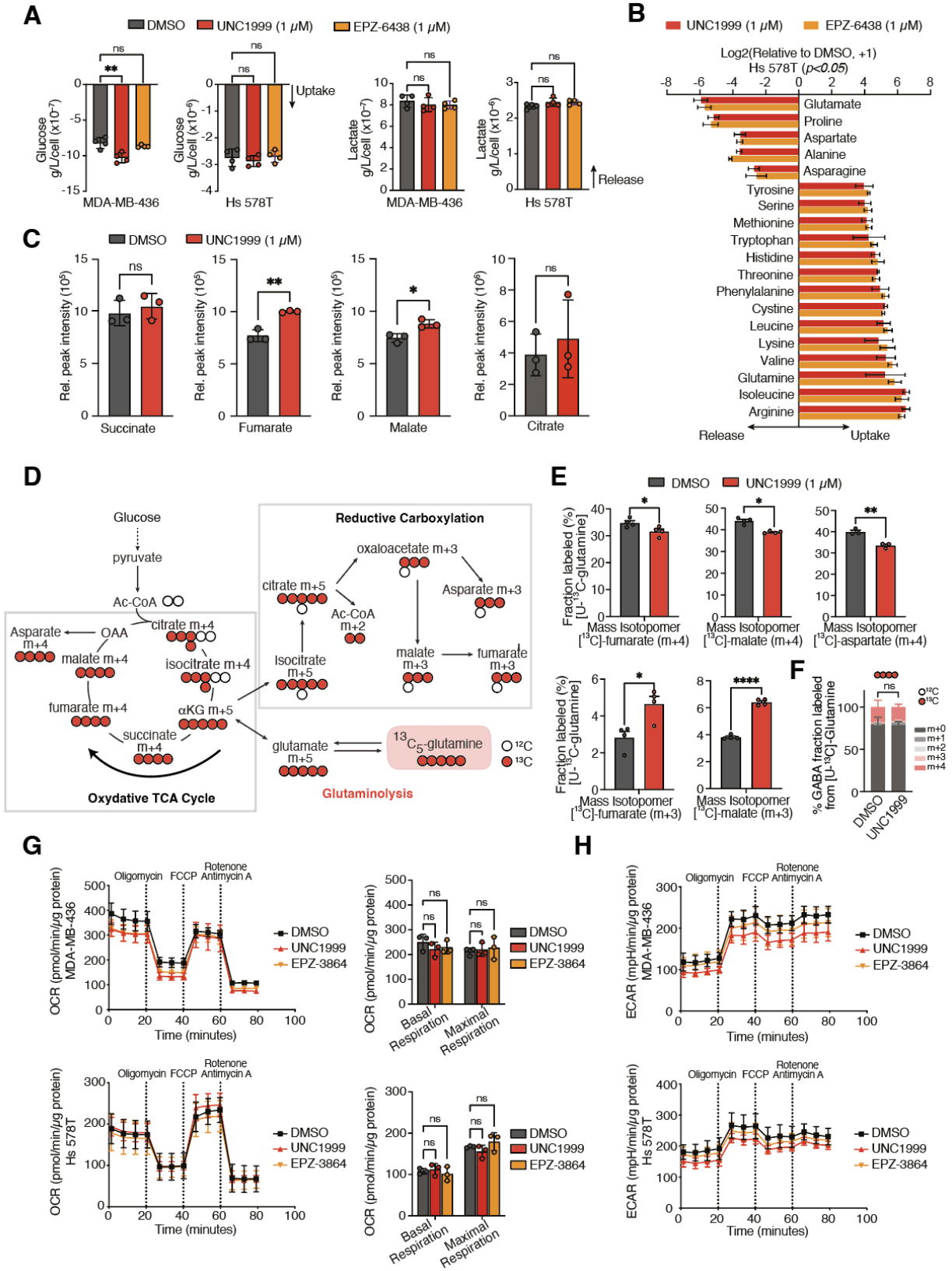

966

967 **Supplementary Figure 4. A.** Relative quantification of glucose and lactate (BioProfile 400, Nova
968 Biomedical) in conditioned media exposed to MDA-MB-436 or Hs 578T cells exposed to
969 UNC1999 or EPZ-6438 (1μM; 72 h) or DMSO (0.2%; N=4; data shown relative to naïve media).
970 **B.** Relative metabolite quantification in conditioned media using QQQ-LC-MS (Intrada-amino-
971 acids) in Hs 578T cells exposed to UNC1999 and EPZ-6438 (1μM; 72 h) or DMSO (0.2%; N=4;
972 $p<0.05$). Metabolite levels for each experimental condition are normalized to those in the naive
973 medium. **C.** Quantification of specific intracellular metabolites in Hs 578T cells by QTOF-LC-
974 MS (Ion-pairing) exposed to UNC1999 (1μM; 72 h) or DMSO (0.2%; N=3). **D.** Schematic
975 representation of the ^{13}C-labeling of glutaminolysis, oxidative TCA cycle, and reductive
976 carboxylation intermediate from $^{13}C_5$-glutamine. **E.** Percentage fraction of ^{13}Carbon-labelled
977 oxidative TCA cycle intermediates (top, fumarate m+4, malate m+4, and aspartate m+4), reductive
978 carboxylation intermediates (bottom, malate m+3, fumarate m+3) in DMSO- and UNC1999-
979 treated (1μM, 96 h) Hs 578T quantified by QTOF-LC-MS (ion pairing) after 2 h exposure to
980 labelled $^{13}C_5$-glutamine (N=4). **F.** Stack bar showing the fraction of ^{13}C-labeled GABA
981 isotopomers in Hs 578T cells exposed to UNC1999 (1μM, 96 h) or DMSO (0.2%; N=4). **G.** Left:
982 Time-dependent Oxygen Consumption Rate (OCR) in MDA-MB-436 (top) and Hs 578T (bottom)
983 cells exposed to UNC1999, EPZ-6438 (1μM; 72 h) or DMSO (0.2%; N=3) upon sequential
984 addition of Oligomycin (1μM), Carbonyl cyanide-p-trifluoromethoxyphenylhydrazone (FCCP;
985 0.5μM) and Rotenone/AntimycinA (0.5μM). Right: Effect of treatment on OCR basal and
986 maximal respiration is plotted. **H.** Time-dependent Extracellular Acidification Rate (ECAR) in
987 MDA-MB-436 (top) and Hs 578T (bottom) cells exposed to UNC1999, EPZ-6438 (1μM; 72 h) or
988 DMSO (0.2%; N=3) upon sequential addition of Oligomycin (1μM), FCCP (0.5μM) and
989 Rotenone/AntimycinA (0.5μM). Data are the mean ± SD from 3 to 4 biological replicates (A, B,
990 C, E, F, G and H). Statistical analysis was performed by two-tailed Student's t test (C, E and F)
991 and one-way ANOVA (A and G). ns, not significant, *$p < 0.05$, **$p < 0.01$, ****$p < 0.0001$.
992

FIGURE S5

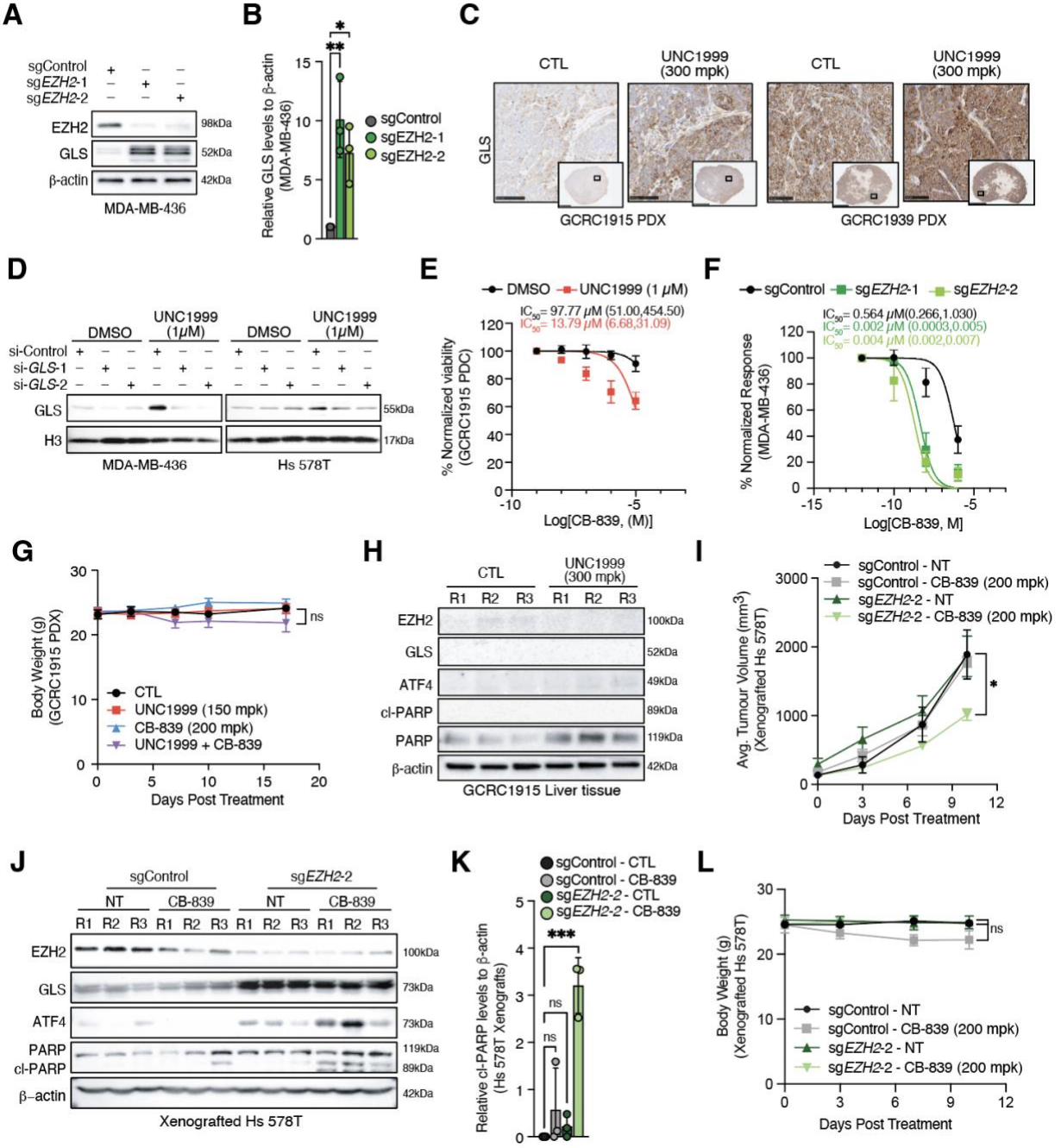

993

994 **Supplementary Figure 5. A.** Immunoblot showing GLS and β-actin levels in MDA-MB-436
995 EZH2 knock-out cells using two different sgRNAs (N=3). **B.** Quantification of the relative GLS
996 levels from Fig. S5A (rel. to β-actin; N=3). **C.** Immuno-histochemistry (IHC) staining for GLS in
997 GCRC1915 and GCRC1939 PDXs exposed or not to UNC1999 (300 mg/kg, 21 days, N=3).
998 Magnification, 20X; scale bars, 100µm. **D.** Immunoblot showing GLS and H3 levels in MDA-
999 MB-436 or Hs 578T cells exposed to UNC1999 (1µM; 96 h) or DMSO (0.2%; N=3) and depleted
1000 of GLS using two siRNAs against *GLS* (96h) vs non-targeting siRNAs (siCtl). **E.** Dose-response
1001 curves representing the relative normalized viability of GCRC1915 PDC cells exposed to DMSO
1002 (0.2%) or UNC1999 (1µM; 120h) (N=3) and co-treated with increasing doses of CB-839. IC50
1003 (95% Confidence Interval) was calculated and indicated at the top of the graph. **F.** Dose-response
1004 curves representing the relative normalized viability of MDA-MB-436 EZH2 knock-out cells and
1005 co-treated with increasing doses of CB-839 (120 h; N=3). IC50 (95% Confidence Interval) was
1006 calculated and indicated at the top of the graph. **G.** Body weight measurements of mice implanted
1007 with GCRC1915-PDX and treated as indicated (control, CB-839 (200 mg/kg; 21 days), UNC1999
1008 (150 mg/kg; 21 days), or combination) over 10 days. **H.** Immunoblot showing the levels of the
1009 EZH2, GLS, ATF4, cl-PARP, and PARP of healthy liver from GCRC1939 PDX exposed to
1010 UNC1999 (300 mg/kg; 21 days) or control (N=3). **I.** Average tumor volume over time of sgControl
1011 and sg*EZH2* Hs 578T xenografted in female NSG mice exposed to CB-839 (200 mg/kg; 10 days)
1012 or control (N=3 per group). **J.** Immunoblot showing the levels of the EZH2, GLS, ATF4, cl-PARP,
1013 PARP, and β-actin in xenografted NSG mice either with sgControl or sg*EZH2* Hs 578T cells
1014 exposed to CB-839 (200 mg/kg; 10 days) or control (N=3). **K.** Quantification of the relative cl-
1015 PARP levels from Fig. S5I (rel. to β-actin; N=3). **L.** Body weight measurements of NGS mice
1016 xenografted with Hs 578T sgControl or sg*EZH2* and treated as indicated in I-J. The data shown
1017 are the mean ± SD from 3 biological replicates (B, E, F, G, K and L); error bars represent SEM for
1018 tumor volume (I). Statistical analysis was performed using one-way (B and K) and two-way
1019 ANOVA (G, I and L). ns, not significant, *$p < 0.05$, **$p < 0.01$, ***$p < 0.001$, ****$p < 0.001$. R:
1020 replicate #.